



HAL
open science

Birefringent metamaterial nanocuboids with tailored optical constants for force and torque transduction

Ying Tang, Seungkyu Ha, Thomas Begou, Julien Lumeau, H Paul Urbach,
Nynke H Dekker, Aurèle J L Adam

► **To cite this version:**

Ying Tang, Seungkyu Ha, Thomas Begou, Julien Lumeau, H Paul Urbach, et al.. Birefringent metamaterial nanocuboids with tailored optical constants for force and torque transduction. ACS Nano, 2020. hal-02996092v1

HAL Id: hal-02996092

<https://amu.hal.science/hal-02996092v1>

Submitted on 9 Nov 2020 (v1), last revised 1 Dec 2020 (v2)

HAL is a multi-disciplinary open access archive for the deposit and dissemination of scientific research documents, whether they are published or not. The documents may come from teaching and research institutions in France or abroad, or from public or private research centers.

L'archive ouverte pluridisciplinaire **HAL**, est destinée au dépôt et à la diffusion de documents scientifiques de niveau recherche, publiés ou non, émanant des établissements d'enseignement et de recherche français ou étrangers, des laboratoires publics ou privés.

Birefringent metamaterial nanocuboids with tailored optical constants for force and torque transduction

Ying Tang^{1,§}, Seungkyu Ha^{2,§}, Thomas Begou³, Julien Lumeau³, H. Paul Urbach¹, Nynke H. Dekker^{2,*}, and Aurèle J. L. Adam^{1,**}

¹Optics Research Group, Department of Imaging Physics, Delft University of Technology, van der Waalsweg 8, 2628 CH Delft, The Netherlands

²Department of Bionanoscience, Kavli Institute of Nanoscience, Delft University of Technology, van der Maasweg 9, 2629 HZ Delft, The Netherlands

³CNRS, Aix-Marseille University, Centrale Marseille, Institut Fresnel, 13397 Marseille, France

*E-mail: n.h.dekker@tudelft.nl

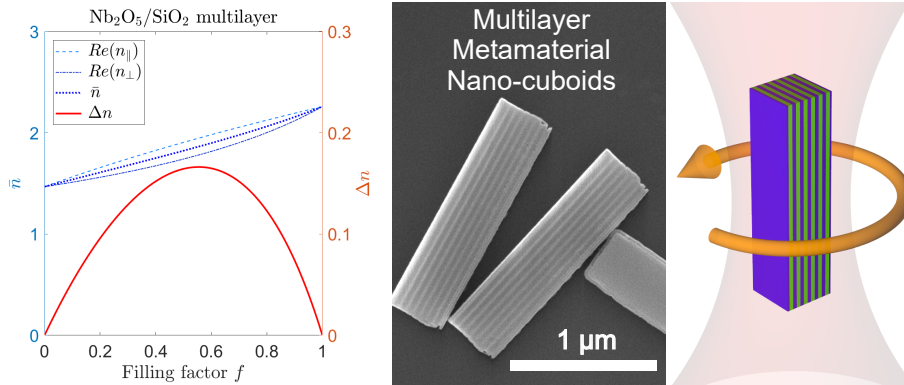
**E-mail: a.j.l.adam@tudelft.nl

§These authors are equally contributed to this work.

Keywords: metamaterial, dielectric multilayer, nanoparticles, optical trapping, force spectroscopy, torque spectroscopy

Abstract

The ability to apply force and torque directly to micro- and nanoscale particles without contact in optical traps has generated wide range of applications in scientific research and engineering. However, most of the particles for such optical manipulations are comprised of a single material that is chosen from the library of naturally available materials. Hence, the design and performance of the particles have been severely constrained by the narrow range of the given set of physical and chemical properties. Here, we overcome these limitations by implementing the concept of dielectric multilayer metamaterial based on the effective medium theory. It allows to obtain a designed combination of refractive index and birefringence suitable for each specific need, by choosing different consisting materials and changing the relative composition ratio of them. Aiming for being highly birefringent yet easily trappable and chemically stable, we have designed and fabricated highly uniform Nb₂O₅/SiO₂-multilayered and square cuboid-shaped nanoparticles. The resulting maximum birefringence is similar to that of calcite CaCO₃ crystal while the refractive index can be as low as that of other common dielectric probes such as silica and polystyrene. These desired properties are successfully demonstrated by tight 3D-trapping and generation of ~ 16 nN·nm torque and ~ 5 kHz rotation frequency at a ~ 100 mW single-beam optical trap in water. This extension to the library of optically trappable materials beyond the existing ones paves the way for further improvements and opportunities in advanced optical manipulation systems.



Graphical Table of Contents

1 Introduction

The development of optical trapping technique has enabled a various of micro- and nanoscale applications over the last decades [1]. The possibility of non-contact optical manipulation and detection of linear and angular motions has offered novel approaches for diverse fields of science and engineering, such as force and torque spectroscopy of single biomolecules [2, 3], quantum optomechanics [4, 5], colloidal self-assembly [6], and optically driven nanomachines [7]. For such utilizations of optical trapping, dielectric materials, e.g., silica and polystyrene (PS) have been popular choices as force transducers [3]. Particularly for the combined manipulation of force and torque, birefringent dielectric probes have proven their advantages over metallic probes [8, 9], enabling direct torque detection, less heating, reduced scattering, and confined rotational degrees of freedom [10]. Therefore, various birefringent dielectrics have been successfully applied as optical force and torque transducers, which are uniaxial crystals such as quartz SiO₂ [11, 12, 13], calcite CaCO₃ [14], vaterite CaCO₃ [15], liquid crystal RM257 [16], and rutile TiO₂ [10] (**Fig. 1a**).

Nonetheless, all of these dielectrics have their own limitations. Silica and PS are commercially available as highly uniform and chemically stable microspheres with wide range of diameters and surface chemistries. However, they are not suitable for torque transducers due to their non-birefringence. Another chemically stable material, quartz SiO₂, is birefringent and allows torque transduction. However, its very low birefringence ($\Delta n = 0.009$) severely limits the transferable torque to the material. Although the torque transfer efficiency can be maximized by enlarging the size of the probe, this not only renders it unfavorable for stable trapping in single-beam optical traps, but also reduces the achievable rotational speed and spatiotemporal resolutions due to the increased viscous drag from the surrounding medium [10]. Calcite and vaterite CaCO₃ have higher birefringence ($\Delta n = 0.1 - 0.16$), however, they are dissoluble in water and therefore less suitable in biological and microfluidic environments.

In contrast, rutile TiO₂ is not only chemically stable in aqueous environments but also has the highest birefringence ($\Delta n = 0.26$) among all the known naturally occurring crystalline materials. In addition, its averaged refractive index ($\bar{n} = 2.6$) is much higher than other common dielectric probes ($\bar{n} = 1.4 - 1.6$). This combination of both exceptional optical index and birefringence allows it to achieve both the highest level of force and torque transfer efficiencies with only a single probe, as well as the excellent measurement precision in force, torque, position, and angle (below 1 pN, 1 pN · nm, 1 nm, and 1 degree, respectively) on short time scales at only moderate laser power [10].

Regardless of the superior properties of rutile TiO₂ as an optical force and torque transducer, it does not provide an omnipotent solution for the wide range of applications. Although the high refractive index of rutile TiO₂ is beneficial to obtain large linear stiffness and force, it results in a large scattering that puts stringent requirements for stable 3D trapping. To generate sufficient gradient force to counteract the scattering force, a tightly focused trapping beam, i.e., high numerical aperture (NA) objective lens, is inevitable. Even with such a tightly focused beam, the probe size has to be limited ($< \sim 300$ nm) in order to restrain the scattering force from exceeding the gradient force [10]. While such requirements are still pertinent to many biological and physical applications, they would become substantial limitations for others in the aspects of optical trapping system designs. First, the flexibility in designing the optics for trapping is substantially diminished. For example, stable 3D trapping of such particles is challenging in compact and affordable optical trapping systems that often possess low NA optics and hence less tightly focused beam [17, 18, 19]. Second, as the 3D trappability of the probes are highly size- and shape-dependent, their use in large size or exotic shape, such as the gear-shaped microfluidic rotors [20, 21], would be impractical. Therefore, the degree of freedom in probe geometry design is severely limited. Third, the high trap stiffness is not beneficial for all cases. A low trap stiffness is intentionally utilized for certain applications, e.g., photonic force microscopy in which a “soft” probe is beneficial to scan a fragile sample such as cell surface [22].

Therefore, beyond the very limited sets of the naturally existing crystalline materials, it is desirable to have a combination of optical constants at will by intentional design. For example, probe particles with low refractive index yet still high birefringence would solve the issues mentioned above. Such tailor-made birefringent particles with optical properties tuned for each specific application are predicted to further broaden the applicability of force and torque transducers in optical trapping.

For a realization of this idea, the concept of metamaterials (MMs) can give a solution. The MMs are engineered materials to confer desired properties that are not possessed by naturally occurring materials. Their abilities to generate artificially defined refractive index [23, 24] and birefringence [25, 26] have been widely demonstrated. Particularly, the multilayer-structure MMs [27] are straightforward to design and implement for both artificial index and birefringence [28, 20]. The fabrication of such multilayer MMs can be achieved readily by sequentially depositing different material layers on a substrate using standard semiconductor fabrication techniques such as sputtering [29], evaporation [30], and atomic layer deposition (ALD) [31]. The lithography, etching, and the sequential harvesting of nanoparticles using a sacrificial layer in fabrication allow to obtain a large number of highly

uniform lithographically-defined MM particles [21, 20, 32, 33]. Moreover, such sacrificial layer-based fabrication is in principle free from the undesired deformation in particle geometry during cleaving them from a substrate [10].

Here, we demonstrate a realization of birefringent multilayer MM particles with designed optical constants, as force and torque transducers in optical traps. Unlike the probe particles fabricated from natural crystals, we can customize the resulting optical properties of the MM particles by choosing multilayer material pairs and the ratio of the layer thicknesses, as demonstrated by means of both theoretical calculations and optical trapping experiments. Aiming for a high birefringence, we have chosen niobium pentoxide (Nb₂O₅) and silicon dioxide (SiO₂) as the consisting multilayer materials. This combination results in a large birefringence at only moderate refractive index, allowing stable 3D trapping with relaxed requirements in optics configuration, particle geometry, and trap stiffness. The resulting optical constants are very close to those of calcite/vaterite CaCO₃. However, unlike CaCO₃ crystals, our MM particles are chemically stable in aqueous environments. Moreover, they are highly uniform and suitable for mass-fabrication.

2 Results and discussion

2.1 Design of birefringent multilayer MM particles

The design principle of the artificially birefringent MM probe is based on the effective medium theory (EMT) [34]. The EMT predicts that a multilayer of alternating isotropic dielectric materials exhibits an effective birefringence. When the thickness of each layer is much smaller than the wavelength of the incident electromagnetic wave, the effective optical permittivity of the structure can be approximated by a tensor

$$\underline{\underline{\epsilon}} = \begin{bmatrix} \epsilon_{\parallel} & 0 & 0 \\ 0 & \epsilon_{\parallel} & 0 \\ 0 & 0 & \epsilon_{\perp} \end{bmatrix}, \quad (1)$$

where ϵ_{\parallel} and ϵ_{\perp} are the permittivity components parallel and perpendicular to the interfacial surfaces of the multilayer stack, respectively. The values of them are given by

$$\epsilon_{\parallel} = \rho\epsilon_1 + (1 - \rho)\epsilon_2, \quad (2)$$

$$\epsilon_{\perp} = \frac{1}{\rho\epsilon_1^{-1} + (1 - \rho)\epsilon_2^{-1}}, \quad (3)$$

where ϵ_1 and ϵ_2 are the permittivity values of the higher- and lower-index materials, respectively, and the material filling ratio $\rho = d_1/(d_1 + d_2)$ is defined as the thickness-ratio of the single higher-index material layer (d_1) and the unit multilayer ($d_1 + d_2$).

To confirm the accuracy of the EMT approximation, we have compared the calculated Fresnel coefficients of the homogeneous single-layer effective medium and the multilayer MM structure in water at our operating wavelength (1064 nm) and target dimensions (calculated by our custom Matlab code according to Ref. [35]; **Fig. S1**). The optical property of the homogeneous single-layer effective medium is calculated by the EMT (**Eq. 1-3**), and the multilayer MM structure uses the nominal optical constants of each consisting layer. In these calculations, we fix the total thickness of both structures as 300 nm, while varying the number of layer-pairs from 1 to 6 in the multilayer geometry. As the number of layer-pairs increases, the Fresnel coefficients calculated from the multilayer geometry approach to those from the single-layer effective medium geometry. The approximated coefficients are highly accurate for 5–6 layer-pairs (the largest deviation from the effective medium is less than 0.4%). This comparison confirms that the EMT is sufficiently precise to describe our multilayer MMs, and we choose 50 nm (= 300 nm \times 1/6) as the thickness of the unit layer-pair for further investigations. Moreover, our finite element method (FEM) calculation validates the EMT as well (**Fig. S2; Methods**).

We have compared diverse combinations of high- and low-index materials for the multilayer (**Fig. S3**). We have focused on the oxide materials as they are commonly available in popular semiconductor thin film fabrication techniques, such as evaporation, sputtering, and ALD, with the capability to form stable multilayer compositions [36]. Also, there exist well-developed surface functionalization protocols for oxide materials, which further facilitate the utilization of multilayer materials in diverse areas including biological applications [37]. We have paired each different high-index material (blue dots in **Fig. S3**) with the low-index material fixed as silicon dioxide (SiO₂) ($n = 1.47$ [38], white dots in **Fig. S3**). It is notable that, depending on the used thin film deposition method and growth parameters, the refractive index of a thin film material can vary and deviate from that of the same material in the bulk crystalline form. For example, the refractive index of the titanium oxide (TiO₂) thin film compared in

Fig. S3 is either 2.07 [39] (prepared by evaporation) or 2.31 [40] (prepared by ALD). We choose niobium pentoxide (Nb_2O_5) ($n = 2.25$ [38]) as the high index material because its index is comparable to that of ALD-prepared TiO_2 film and higher than aluminum oxide (Al_2O_3) ($n = 1.67$ [41]) and hafnium oxide (HfO_2) ($n = 2.08$ [42]) films. Also, its multilayer composition with SiO_2 has been successfully demonstrated for optical applications and can be reliably fabricated by us [36]. We use plasma-assisted reactive magnetron sputtering (**Methods**) and the refractive index measurements on the deposited films reveal the expected values, i.e., $n = 2.26$ for Nb_2O_5 and $n = 1.47$ for SiO_2 at 1064 nm.

The effective birefringence and the corresponding averaged refractive index of each material combination can be predicted using the EMT (**Eq. 1-3**), as a function of material filling ratio ρ . In **Fig. 1b**, the calculation result is shown for the case of $\text{Nb}_2\text{O}_5/\text{SiO}_2$ multilayer. The refractive index component n_{\parallel} ($= \sqrt{\epsilon_{\parallel}}$) is a straight line (light blue dashed line), while the refractive index component n_{\perp} ($= \sqrt{\epsilon_{\perp}}$) is a bent curve (dark blue dash-dotted curve) whose value is always the same as or smaller than n_{\parallel} . The averaged index \bar{n} is displayed as the dotted blue curve, while the magnitude of the difference between them (Δn) is shown as the red curve, indicating a negative uniaxial birefringence with $n_e = n_{\perp} < n_o = n_{\parallel}$. In order to maintain the desired orientation and provide proper rotational control of the particle in an optical trap (**Fig. 1c**), the particle is designed to be square cuboid shape with high aspect ratio (AR) (3–6) (**Fig. 1d**). The high AR generates sufficiently large geometrical torque [10] around the x - and y -axis and maintain the particle orientation in the y - z and x - z plane, respectively, as shown in **Fig. 1c**. Therefore, the rotary control of the particle around the z -axis can be achieved by utilizing its birefringence in the x - y plane that originates from the multilayer structure. Although the cross section of a square cuboid is not rotationally symmetric as like that of cylinders [11, 43, 44, 10], it minimizes the geometrical torque around the z -axis when compared to a rectangular cuboid. Hence, the particle rotation around the z -axis can be mainly controlled by manipulating the polarization direction of the linearly polarized input beam.

The EMT (**Eq. 1-3**) also offers general guidelines to design optical constants of multilayer MMs by will. Taking the $\text{Nb}_2\text{O}_5/\text{SiO}_2$ multilayer as an example (**Fig. 1b**), the effective birefringence (Δn) of the MM can be selected between zero and the maximum (0.17 when $\rho = 0.55$, similar to that of calcite crystal) by choosing the corresponding filling ratio ρ of the multilayer. Meanwhile, depending on the chosen filling ratio, the averaged refractive index (\bar{n}) of the MM varies between 1.47 (that of low index material, SiO_2) and 2.25 (that of high index material, Nb_2O_5). Except the case of the maximum birefringence, there exist two filling ratios with which the same level of birefringence can be obtained. These two possible choices form a trade-off relationship between the particle trappability and the maximal force generation. A smaller index renders the MM particle to be more easily trapped in 3D due to the reduced scattering force, while a larger index brings enhancement in gradient force due to the increased index contrast with the surrounding medium (i.e., water in our experiments). Therefore, depending on the target application or the given experimental situation, one can determine the suitable material filling ratio to obtain a desired combination of refractive index and birefringence for MM particles (e.g., “high \bar{n} & high Δn ” pair or “low \bar{n} & high Δn ” pair).

Considering the above-mentioned guidelines based on the EMT and the feasibility of particle realization through fabrication, we have chosen two different filling ratios ($\rho = 0.3$ and $\rho = 0.5$) to demonstrate the tunability of the optical constants of our MM particles (for a more straightforward calculation and fabrication, we confine the precision of ρ values to the first decimal). We take $\rho = 0.5$, close to $\rho = 0.55$ that maximizes birefringence as mentioned above, to target a large birefringence ($\Delta n = 0.16$, while average index \bar{n} becomes 1.82), being ~ 18 times larger than that of quartz crystal ($\Delta n = 0.009$). Then, we choose $\rho = 0.3$ as the second option, aiming for a lower index ($\bar{n} = 1.68$) to further facilitate 3D trapping with a still high enough birefringence ($\Delta n = 0.13$, ~ 14 times larger than that of quartz). Notably, using the filling ratio ρ as the only tuning parameter, the $\text{Nb}_2\text{O}_5/\text{SiO}_2$ multilayer can have a birefringence as high as that of calcite ($\Delta n = 0.16$, $\bar{n} = 1.56$), and a refractive index as low as that of vaterite ($\Delta n = 0.1$, $\bar{n} = 1.6$) and many other common dielectric materials for trapping ($\bar{n} = 1.4 - 1.6$). Overall, this multilayer with $\rho = 0.3 - 0.5$ can realize the combination of moderate index and high birefringence (“low \bar{n} & high Δn ” system) as like calcite/vaterite CaCO_3 , being complementary to rutile (which is a “high \bar{n} & high Δn ” system) as discussed in the introduction. If obtaining a higher linear stiffness is of interest as like rutile, selecting only a higher filling ratio ($\rho = 0.5 - 0.8$) is sufficient to obtain the same level of birefringence with an increased index as high as $\bar{n} = 2.1$ (**Fig. 1b**).

In this section, we have determined most of the design parameters for our multilayer MM particles. We choose Nb_2O_5 and SiO_2 as the paired materials to compose the multilayer, with 50 nm as the unit-pair thickness. We focus on two different material filling ratios (0.3 and 0.5), which result in two distinct sets of optical constants. For the geometry of each particle, we use a square cuboid with high AR . The specific dimensions (i.e, width and height) of the nano-cuboids are determined based on the FEM-calculated optical trapping landscapes in the following section.

2.2 Numerically calculated trapping performance of multilayer MM particles

The FEM-calculations of optical trapping landscapes offer inevitable insights into the predicted performance of our multilayer MM particles, for both linear and angular manipulations, as a function of particle dimensions. We determine the dimensional range of the particles for calculation as follows. First, we explore the total multilayer thickness (i.e., width of nano-cuboids) starting from $W = 250$ nm (up to $W = 450$ nm). The thickness of the unit layer-pair is fixed as 50 nm, and hence every particle has a large enough number of multilayer pairs (≥ 5), for which the EMT results in highly precise approximation as discussed in the previous section. Second, for AR , we study from the cube ($AR = 1$) to the square cuboids with different heights (AR up to 7). The resulting range of heights ($\sim 0.5 - 3$ μm) include the height for the 100% torque transfer efficiency [10] for each filling ratio (2.1 μm for $\rho = 0.3$ and 1.6 μm for $\rho = 0.5$; **Fig. S4**).

To diagnose the 3D-trappability and predict the maximal axial trapping force of MM particles in square cuboid geometry, we have calculated the axial stiffness κ_z for $\rho = 0.3$ and $\rho = 0.5$ (**Fig. 2a,b**). For each particle dimension, κ_z is defined as the slope of the axial force curve at the equilibrium trapping position (z_{eq} ; **Fig. S5**). The nano-cuboids with $\rho = 0.3$ are trappable for the entire calculation range of width ($W = 250 - 450$ nm) and aspect ratio ($AR = 1 - 7$). In contrast, the nano-cuboids with $\rho = 0.5$ include the non-trappable dimensions (appear from $W \approx 380$ nm) displayed as the black pixels in **Fig. 2b**, for which the axial stiffnesses are not defined due to the dominant scattering forces and the resulting absence of z_{eq} (therefore, the corresponding dimensions are not used for the following calculations and displayed as black pixels as well in **Fig. 2d** and **Fig. 3b,d**). Our additional calculation with an extended width range (W up to 550 nm; **Fig. S6**) shows that the nano-cuboids with $\rho = 0.3$ starts to have non-trappable dimensions only from $W \approx 525$ nm. The narrower range of 3D-trappable dimensions for the MM particles with $\rho = 0.5$ is due to the larger scattering force from their higher effective refractive index ($\bar{n} = 1.82$), compared to that of the MM particles with $\rho = 0.3$ ($\bar{n} = 1.68$). As a trade-off of this reduction in the trappable dimensions, the higher index of $\rho = 0.5$ particles allows a more effective linear momentum transfer. For example, the similar κ_z (~ 1.4 pN/ $\mu\text{m}/\text{mW}$) can be achieved with $\sim 40\%$ smaller volume of a particle with $\rho = 0.5$ ($W = 340$ nm, $AR = 3.4$; magenta circle in **Fig. 2b**), compared to that of a particle with $\rho = 0.3$ ($W = 450$ nm, $AR = 2.5$; magenta circle in **Fig. 2a**). It is noteworthy that, regardless of the filling ratios, these axial stiffness maxima are achieved when a particle has height close to $\sim 1.1 - 1.2$ μm and is also centered around the beam focus ($z_{eq} \approx 0$ nm; **Fig. S5**). This trend is clearly visualized by the stiffness maxima calculated per each particle width (red squares in **Fig. 2a,b**), which forms almost an equal-height curve in each κ_z map. This correlation is presumably due to the optimal overlap of the particle volume and the focus beam volume, in which the largest field gradient can be experienced by the particle.

When it comes to the lateral stiffness, we calculated κ_y (**Fig. 2c,d**) at z_{eq} , which is larger than κ_x when the input beam is linearly polarized along the x -axis [10]. The κ_y is maximized around $W \approx 300$ nm (the most bright regions in **Fig. 2c,d**) regardless of the chosen filling ratios, and the κ_y maxima (~ 11 pN/ $\mu\text{m}/\text{mW}$) also appear at $W \approx 300$ nm ($AR \approx 5$) (magenta circles in **Fig. 2c,d**). The existence of this optimal particle width for lateral force is considered as a result of the ideal overlapping with the focus volume along the lateral direction, similarly as the case of axial trapping. Overall, the lateral stiffness is almost an order of magnitude larger than the axial stiffness, due to the absence of the net lateral scattering forces [10].

The calculated maps of angular stiffness κ_θ (**Fig. 3a,b**) represent the maximum torque ($\tau_o = k_\theta/2$), which is experienced by a particle rotated 45° with respect to the input beam linear polarization direction. The maxima of κ_θ calculated per each particle width (red squares in **Fig. 3a,b**) are distributed around $H \approx 2.5 - 2.6$ μm for $\rho = 0.3$ and $H \approx 2.0 - 2.1$ μm for $\rho = 0.5$. These heights for the optimal torque transfer efficiency are ~ 0.5 μm larger than those predicted by the ideal theory (equation 1 of Ref. [10]; $H = 2.1$ μm for $\rho = 0.3$ and $H = 1.6$ μm for $\rho = 0.5$ as shown in **Fig. S4**), which is attributed to the peculiarities of nanoparticle trapping with a tightly focused beam that are not considered in the ideal equation [10]. Overall, within the same range of dimensions chosen for the calculation of κ_θ maps, the particles with $\rho = 0.5$ have larger angular stiffness values (maximum κ_θ of 877 pN·nm/rad/mW) than those of the particles with $\rho = 0.3$ (maximum κ_θ of 653 pN·nm/rad/mW). This enhanced torque of $\rho = 0.5$ particles is a consequence of their 27% higher birefringence than that of $\rho = 0.3$ particles.

Although the angular stiffness of $\rho = 0.5$ nano-cuboids can be maximized with the particle dimensions on the finger-shaped regions [45] (for example, the maximum κ_θ at $W = 445$, $AR = 4.6$, as marked with the magenta circle in **Fig. 3b**), their utilization is difficult in practice for the applications that require 3D trapping. First, some fraction of the fabricated particles can be easily outside of the finger region due to the distributions in the actual particle dimensions, and fall onto the regions of black pixels that do not support 3D trapping. Second, the non-idealities of the actual trapping system (e.g., aberration of the focus beam) will modify the trapping landscape (e.g., shift of the finger regions or the threshold diameter for 3D trapping) [10], and hence even the particles fabricated

with high uniformity might have less stiffness or become non-trappable. In contrast, as a trade-off of being less efficient in torque transfer, nano-cuboids of $\rho = 0.3$ can be trapped in 3D for every dimension shown in the map due to their lower refractive index, including the dimension for the maximum κ_θ ($W = 445$, $AR = 5.6$).

In **Fig. 3c,d**, we show the angular speed f_o ($= (k_\theta/2)/(2\pi\gamma_\theta)$) maps for the nano-cuboids, calculated using the maps of κ_θ and rotational drag coefficient γ_θ (which is also FEM-calculated; **Fig. S7**). Overall, the larger angular speeds are achieved with smaller dimensions (e.g., the maxima for both maps appear at $W = 255$ nm, $AR = 3.7$), due to the fact that the rotation of larger particles is severely hindered by the increased rotational drag in the surrounding medium (water). Meanwhile, the larger angular stiffnesses of the particles with $\rho = 0.5$ allow faster angular rotation speeds (maximum f_o of 61 Hz/mW) than those of the particles with $\rho = 0.3$ (maximum f_o of 45 Hz/mW). For both material filling ratios, the maximum speed for each particle width is distributed around the equal-height line of ~ 1 μm , where the optimal balance between the angular stiffness and drag are achieved to maximize the speed.

Based on these numerical calculation results, we have finalized the multilayer MM particle dimensions for fabrication (**Methods**). For the smaller filling ratio $\rho = 0.3$, we fabricated one wafer with $W = 300$ nm (wafer A) and another wafer with $W = 400$ nm (wafer B), because particles with these widths are expected to be stably 3D-trappable. For the larger filling ratio $\rho = 0.5$, we fabricated only one wafer with $W = 300$ nm (wafer C), considering the smaller 3D trapping threshold diameter (**Fig. 2b**). We choose AR of 3, 4, and 5 for all three wafers A–C to obtain particle heights H covering the sufficiently wide range of $\sim 1 - 2$ μm . Therefore, the resulting heights include those for achieving highly optimized torque transfer efficiency with each material filling ratio, i.e., $H = 2.0$ μm for $\rho = 0.3$ ($W = 400$ nm, $AR = 5$) and $H = 1.5$ μm for $\rho = 0.5$ ($W = 300$ nm, $AR = 5$) (**Fig. S4**). We also fabricated particles with $AR = 6$ ($H = 1.8$ μm) from wafer C, to explore the torque behavior of particles longer than the theoretically optimal height for torque transfer ($H = 1.6$ μm). The dimensions of the designed sample batches are indicated by the corresponding symbols and labels in **Fig. 2a,b**, where the alphabet and number in each label represent the wafer and the aspect ratio, respectively.

2.3 Linear and angular trapping behaviors of multilayer MM particles

We have fabricated ten batches of multilayer MM particles in total (**Methods**; **Fig. S8,S9,S10**; **Table. S1**), as designed above (A3–5, B3–5, and C3–6), and measured them in an optical torque wrench setup (**Methods**; **Fig. S11**; **Table. S2**) with which both linear and angular trapping properties can be characterized [10]. The fabrication process has been tuned to produce particles with actual dimensions as close as possible to the design parameters and have overall deviations less than $\sim 5\%$ in the width and height (**Fig. S10**), while the thickness is precisely controlled during multilayer deposition (**Fig. S9**).

The tight 3D-trappability of the nano-cuboids has been confirmed by measuring linear stiffness values in all principal axes (x , y , and z) (**Fig. S12**). As expected for optical trapping with single-beam that is linearly polarized along the x -axis [46], measured nano-cuboids show the highest stiffness along the y -axis (κ_y), and we use the lateral trapping data from the measurements along the y -axis in the following analysis. Each 3D-trapped nano-cuboid further reveals the angular trapping characteristics by modulating the linear polarization direction of the input beam (**Methods**). The measured linear and angular stiffness values of the nano-cuboids are shown in **Fig. 4a,b**. The particles within each batch behave very consistently, with small relative standard deviations ($\text{RSD} = \text{SD}/\text{mean} \times 100$) in both measured linear and angular stiffnesses ($\text{RSD} = 6\% \pm 5\%$; mean and SD are calculated from the entire ten particle batches). The measured linear and angular drag coefficients also show very small variations among different particles within each batch ($\text{RSD} = 5\% \pm 4\%$). These RSD values are comparable to those of the commercial standard PS beads measured in our setup ($\text{RSD} = 8\% \pm 1\%$ for stiffness and $\text{RSD} = 9\% \pm 2\%$ for drag) and confirm that the fabricated multilayer nano-cuboids are highly uniform in both optical properties and geometry.

The measured linear and angular stiffnesses show quantitative agreement with the corresponding FEM calculated values scaled by $59\% \pm 22\%$. This scaling factor is expected as no optical aberration is considered in the FEM calculations, which can substantially distort the field gradient of the focus beam in an implementation of trapping optics. The similar scaling factors have been observed for other probe materials ($58\% \pm 7\%$ of polystyrene beads and $42\% \pm 14\%$ of rutile TiO_2 cylinders) as well in the same setup [10]. Meanwhile, the measured linear and angular drag coefficients agree with the FEM calculated drags scaled by $76\% \pm 13\%$ (**Fig. S13**), unlike the highly exact agreement which has been observed for spherical ($102\% \pm 8\%$; linear drag) and cylindrical ($104\% \pm 17\%$; both linear and angular drag) geometries in the same setup [10]. This difference is attributed to the fact that each nano-cuboid is modeled as an ideal square cuboid with sharp edges, while in reality the fabricated particles have rounded edges (**Fig. S10**) that might reduce the actual drag experienced by the particles.

Although the particles of A3–5 and C3–5 batches have the same design geometry ($W = 300$ nm, $AR = 3 - 5$)

and hence the similar drag coefficients as shown in **Fig. S13**, their measured linear and angular stiffness values are distinguishable each other because of their different material filling ratios. As predicted by the EMT, the wafer C ($\rho = 0.5$) has 9% and 27% larger index and birefringence than wafer A ($\rho = 0.3$), respectively. Consequently, the particles of C3–5 batches ($\rho = 0.5$) exhibit measured linear and angular stiffnesses that are $\sim 29\%$ and $\sim 40\%$ higher than A3–5 batches ($\rho = 0.3$), respectively. These trends match well with our theoretical predictions in which larger index and birefringence lead to higher force and torque (**Fig. 2,3**), proving that the optical constants of multilayer structures can be tuned by the filling ratio.

While increasing AR from 3 to 5 results in higher force and torque for C3–5 batches, the torque transfer efficiency becomes saturated from the particle height that corresponds to C5 batch, as evidenced by the only slight increase in angular stiffness from C5 to C6. This behavior is similar to the predictions by the ideal equation (**Fig. S4**) and the FEM-calculation (**Fig. 3b**). If much higher torque than this saturated level is desired, then enlarging the particle width W can be considered instead of further increasing AR . However, such approach is limited in the case of wafer C ($\rho = 0.5$), because the range of width for 3D-trappability is narrower due to its higher index (**Fig. 2b**). Here, tuning optical constants can provide a solution. As the lower index of $\rho = 0.3$ wafers expands the range of 3D-trappable particle dimensions while still providing a comparably high birefringence, much larger particles can be stably trapped and utilized to generate a large torque. For example, although B3–5 particles have a slightly smaller birefringence than the particles of C3–5 batches, their larger trappable sizes ($W = 400$ nm) eventually allow to obtain higher torque than C3–5 ($W = 300$ nm), as shown in **Fig. 4b**. Particularly, with B5 particles ($W = 400$ nm, $AR = 5$) whose height is close to the theoretical optimum for the torque transfer efficiency of $\rho = 0.3$ multilayer (**Fig. S4**), $\sim 23\%$ larger torque can be obtained than that of the optimal-height particles from $\rho = 0.5$ wafer with $W = 300$ nm (C5–6).

In addition to the stiffness and drag, another parameter describing the trapping performance of particles is the response time t_c which can be defined as the ratio of the measured drag and stiffness (i.e., the slope of the fitted lines in **Fig. 4c,d**). This trap relaxation time is inversely proportional to the laser beam power and therefore can be further shortened by using a higher beam power (here, we assume 100 mW). We benchmark the response times of multilayer MM particles with those from PS beads and rutile TiO₂ cylinders which have been measured in the same setup [10] (**Fig. 4c,d**). We have performed separate linear fitting for each dataset grouped by the material filling ratio of either 0.3 or 0.5, as they are effectively two different materials with distinguishable optical constants. The linear response time of $\rho = 0.5$ particles (wafer C; $t_{c,y} = \sim 11$ μ s) is superior than those of $\rho = 0.3$ particles (wafers A and B; $t_{c,y} = \sim 14$ μ s) and PS beads ($t_{c,y} = \sim 26$ μ s), being nearly the same as that of rutile TiO₂ particles ($t_{c,y} = \sim 11$ μ s). The angular response time of $\rho = 0.5$ particles ($t_{c,\theta} = \sim 18$ μ s) is also very close to that of rutile ($t_{c,\theta} = \sim 15$ μ s) and enhanced by two times with respect to that of $\rho = 0.3$ particles ($t_{c,\theta} = \sim 35$ μ s). These distinguishable response times between the $\rho = 0.3$ and $\rho = 0.5$ particles clearly prove again that both index and birefringence of multilayer structures can be successfully tuned by choosing different material filling ratios.

The capability of generating high torque due to both the high birefringence and the large size of 3D trappable particles is intuitively represented by the measured torque-speed curves (**Fig. 5**; measured at 92 mW beam power in water). The optical torque is shown as a function of the linear polarization rotation frequency (PRF) of the input beam, and the particle rotation frequency is identical to the PRF while the PRF scans from zero to the threshold PRF that results in the maximum torque. Hence, the slope of the linear part of each curve represents the angular drag coefficient ($\gamma_\theta = \tau_o / (2\pi f_o)$) of the corresponding particle. As compared above, the particles of A3–5 and C3–5 batches have similar angular drag coefficients due to the same design geometry, which is clearly represented by the nearly identical slopes of the linear region of the torque-speed curves in **Fig. 5**. However, the higher birefringence of C3–5 batches allows to obtain both larger maximum torque and angular speed. Meanwhile, the torque transfer efficiency becomes maximized and saturated from the height of the particle C5, and hence the further increased height of particle C6 contributes to only smaller torque enhancement compared to those observed from C3–4 and C4–5 particles. Although $\rho = 0.3$ particles exhibit lower birefringence than $\rho = 0.5$ particles, the lower index of $\rho = 0.3$ structure allows to 3D-trap much larger particles (B3–5) and obtain torque even higher than those from $\rho = 0.5$ particles (C3–6). For example, the B5 particle can generate a torque as high as 16.3 nN·nm which is larger than the highest torque among C3–6 particles (13.5 nN·nm from the C6 particle). As a trade-off, the larger angular drag of B3–5 particles decreases their achievable maximum angular frequency values than those of C3–6 particles. As an example, the B3 particle exhibits the maximum torque (13.2 nN·nm) which is close to that of C6 but slower maximum rotation frequency (2.2 kHz) than that of C6 (3.6 kHz).

We also benchmark the torque-speed performance of multilayer MM particles with that of rutile TiO₂ single-crystal particles (red circles in **Fig. 5**) measured in the same setup and conditions (data from Ref. [10]), in the aspect of the torque-speed space that can be covered by each material system. The MM particles can achieve 1.7–2 times higher maximum torque (16.3 nN·nm for $\rho = 0.3$; 13.5 nN·nm for $\rho = 0.5$) than that of rutile TiO₂ (maximum

of 8.0 nN·nm), because the MM particles could compensate their lower birefringence by using larger particles (with 300 – 400 nm-diameter) which exceed the threshold diameter for 3D trapping of rutile TiO₂ particles (~260 nm; the particle diameter ranges in 160 – 230 nm for the presented dataset). Meanwhile, the maximum angular speed of the MM particles (3.5 kHz for $\rho = 0.3$, 5.0 kHz for $\rho = 0.5$) is slower than that of rutile TiO₂ (7.6 kHz) due to the increased drag from their larger sizes.

3 Conclusion

In this work, we have demonstrated a robust approach to design and fabricate free-floating multilayer MM nanoparticles, further extending the library of materials suitable for force and torque transduction. We have validated the accuracy of the EMT approximation for predicting the optical constants of multilayer structures, by analytical and numerical calculations. We choose the multilayer of Nb₂O₅ and SiO₂ as the material system for experimental demonstration of our approach, among many potential material combinations, and achieve high birefringence with moderate refractive index. With this material system, optical constants can be tuned in a wide range (refractive index $\bar{n} = 1.46 - 2.26$ and birefringence $\Delta n = 0 - 0.17$) as a function of material filling ratio. Particularly, its maximum possible birefringence is as high as that of calcite CaCO₃ crystal ($\Delta n = 0.16$), and its refractive index is as low as that of vaterite CaCO₃ ($\bar{n} = 1.6$) and other common dielectric materials ($\bar{n} = 1.4 - 1.6$). The linear and angular trapping properties of square cuboid-shaped nanoparticles made of this multilayer MM are anticipated by the FEM calculations, as a function of particle dimension and material filling ratio. Our designed nano-cuboids are fabricated by a top-down protocol, using etching into a multilayer stack made of alternating Nb₂O₅ and SiO₂ subwavelength-thickness layers (i.e., 6 or 8 layer-pairs with unit layer-pair thickness of 50 nm). The particles are directly dispersible into pure water from their substrate by dissolving the underlying sacrificial layer, and indissoluble in water, thereby compatible with microfluidics and biological applications in contrast to several high-birefringence crystals such as calcite and vaterite CaCO₃.

The tunability of the optical constants according to the EMT have been proven experimentally by the characterization of the linear and angular trapping properties of our fabricated nano-cuboids in an optical torque wrench. As predicted, the particles with the material filling ratio $\rho = 0.5$, which exhibit a maximized birefringence in the Nb₂O₅/SiO₂ multilayer system, have been proved to possess indeed higher index and birefringence over $\rho = 0.3$ particles with the same dimensions (inferred from their higher linear and angular stiffnesses, respectively, regardless of their similar drags). However, the best torque could have been achieved with $\rho = 0.3$ particles as their lower index enables 3D trapping of larger particles, with a trade-off of being slower due to larger drags. When benchmarked with the nanocylinders made of rutile TiO₂ single-crystal that has the highest birefringence among the known crystalline dielectrics [10], MM nano-cuboids have twice larger best torque (~16 nN·nm at ~100 mW in water) as their lower birefringence is able to be compensated by the possibility of using larger dimensions (and hence with the smaller best rotation frequency (~5 kHz)). Meanwhile, the measured response times, particularly for $\rho = 0.5$ particles (10 – 20 μ s at 100 mW), are similarly short as those of rutile TiO₂ particles and prove that our MM nano-cuboids exhibit high linear and angular momentum transfer efficiencies that are reasonable for their predicted optical constants. Moreover, the variations of the measured stiffness and drag are as small as the commercial standard PS beads, demonstrating both highly uniform optical properties and dimensions of our fabricated particles.

Our demonstrated approach for the realization of birefringent MM particles are expected to pave the way for further extending optical trapping-based applications with controllable force and torque levels, as such material system has various advantages over existing materials as follows. First, the user can fine-tune the desired combination of index and birefringence for each specific application, overcoming the very limited options available in the naturally occurring materials only. For example, highly birefringent yet 3D-trappable large particles (e.g., Nb₂O₅/SiO₂ multilayer with $\rho = 0.3$ as shown here) would be promising as powerful rotating microfluidic components [20]. Moreover, the large number of potential material combinations will further broaden the achievable range of optical constants, beyond that of Nb₂O₅/SiO₂-pair which is demonstrated here. Second, the high stability in aqueous environment and the possibility of surface functionalization [33] are beneficial for biological applications including molecular rotary motor studies [47]. Third, the optic axis perpendicular to the multilayer substrate surface allows high flexibility in fabricable birefringent particle geometry, with practically no limit in the obtainable particle height (which largely affects the torque transfer efficiency as demonstrated here with particles of different aspect ratios) and sidewall shape (from straight to even non-symmetric shapes [48]). In contrast, for the birefringent substrate with the optic axis parallel to it, rotatable particles are fabricated by vertical etching and hence particles with large height ($\geq 1 - 2 \mu$ m) or unconventional sidewall shape are technically difficult to realize [49]. Fourth, the sacrificial layer-based fabrication is suitable for mass fabrication and allows highly uniform

particle geometry due to the absence of mechanical cleaving of particles, unlike the single crystal substrate-based fabrication (e.g. quartz [12] or rutile [10]). This is advantageous for various torque-related biological [50] and physical [4] experiments in which a large number of identical particles is desired to obtain statistically sound and reproducible results.

Methods

Finite element method modeling of optical trapping behaviors and hydrodynamic drag

The finite element method (FEM) (COMSOL Multiphysics 5.2a) is used to calculate the optical response of multilayer MM particles. A square cuboid-shaped particle is surrounded by a uniform medium (water, $n = 1.33$) of spherical shape, which is terminated by a perfectly matched layer (PML) shell. The scattering of the particle is calculated under the background illumination of highly focused Gaussian beam (linearly polarized along the x -axis) which is described by the diffraction integral of Richards and Wolf [51, 52]. The vacuum wavelength of 1064 nm, numerical aperture (NA) of 1.2, and aperture filling ratio of 1.7 are used, which are the same as the configuration of our experimental setup [10]. The optical force and torque are retrieved by integrating Maxwell stress tensor (MST) on the surface of a virtual sphere enclosing the MM particle [53].

For modeling the inner structure of a square cuboid particle, we use the single-layer structure with effective optical constants (predicted by the EMT) for the calculation of the optical trapping maps (**Fig. 2,3**) rather than the actual multilayer structure, as the calculation time can be substantially reduced. This approach has been validated by calculating the axial trapping force from both structures for comparison, where the resulting force curves show only negligible differences (**Fig. S2**). This comparison also confirms that the EMT is a sufficiently precise description for our subwavelength multilayer structures at the operating wavelength of 1064 nm.

The viscous drag coefficients are also calculated by FEM (computational fluid dynamics (CFD) module of COMSOL). The surrounding medium (i.e., water) is set to flow translationally (rotationally), inducing viscous drag force (torque) on the MM particle located at the center of the calculation domain. The solutions of Navier-Stokes equations result in force and torque as a function of the speed of the medium flow, from which the linear (rotational) drag coefficients are extracted.

These FEM models are validated in our previous report [10] to model rutile TiO₂ cylinders and only updated to use a square cuboid as the particle geometry instead of a cylinder.

Fabrication of multilayer MM particles

The multilayer MM particles are fabricated using a top-down fabrication process (**Fig. S8**), which is adapted from our previous work [49, 10]. First, a four-inch silicon (Si) wafer is cleaned with fuming (99.5%) HNO₃ (10 min), followed by thoroughly washing with DI and spin-drying (**Fig. S8a**). Next, a 100 nm-thick sacrificial chromium (Cr) layer is deposited on the Si wafer by electron-beam evaporation (FC-2000, Temescal) with the film deposition rate of 0.5 Å/s at the chamber pressure of $\sim 3 \times 10^{-7}$ Torr (**Fig. S8b**). This slow deposition allows to obtain a high-quality Cr-coating with small surface roughness. Then, the Nb₂O₅/SiO₂ multilayer is deposited using plasma-assisted reactive magnetron sputtering (HELIOS, Bühler) (**Fig. S8c**), with which the layer thicknesses are precisely controlled with the aid of in-situ optical monitoring (**Fig. S9**). The whole multilayer stack is designed to be symmetric by starting and finishing with SiO₂ layers. The detailed multilayer composition of the fabricated samples are described in **Table S1**.

The particles of square cuboid geometry are shaped by lithography and etching with Cr hard mask. The substrate is first machine-diced to 1 cm \times 1 cm sizes, which are then cleaned with HNO₃ and DI, as like the Si wafer preparation step. Then, the samples are further cleaned in an ultrasonic bath with acetone (5 min) and isopropyl alcohol (IPA, 5 min), and spin-dried. A layer of ~ 250 nm-thick positive-tone electron-beam resist (AR-P 6200.9, Allresist) is spin-coated (**Fig. S8d**) and patterned by electron-beam lithography (EBPG 5000+, Vistec) with an exposure dose of 240 $\mu\text{C}/\text{cm}^2$ (**Fig. S8e**). The particles are patterned in a hexagonal array (**Fig. S10**), with a large enough gap size (1 μm) between adjacent particles for a more complete Cr lift-off with adhesive tape and an improved wetting with Cr wet etchant in the later steps. The development of the patterned resist layer is performed with ultrasonication, sequentially dipping the sample in pentyl acetate (2 min), 1:1 mixture of methyl isobutyl ketone (MIBK) and IPA (1 min), and then IPA (1 min), followed by spin-drying. A hard etch mask layer (~ 70 nm-thick Cr) is deposited by argon (Ar)-plasma sputtering (AC450, Alliance Concept), with radio frequency (RF) power of 100 W, Ar supply of 20 sccm, and chamber pressure of 100 μbar (**Fig. S8f**). This sputtering condition is optimized for conformal deposition of Cr, allowing the enhanced etch mask shape which results in more vertical sidewalls after etching [10]. For lift-off, adhesive tape (Kapton) is initially used

to remove most of the top Cr layer, and then the remaining resist layer is removed by dipping the sample in PRS-3000 (J.T.Baker) resist stripper at 80 °C for 30 min (**Fig. S8g**). After rinsing the sample thoroughly with DI and spin-drying, a reactive ion etcher (RIE; Fluor Z401S, Leybold Hereaus) is used for etching the multilayer vertically (**Fig. S8h**). The mixture of CHF₃ (50 sccm) and O₂ (3 sccm) is used for this dry etching [49], in which the chamber pressure and the RF power are 50 μ bar and 200 W, respectively (resulting the multilayer etch rate of \sim 50 nm/min). For ensuring the complete removal of the multilayer film within the unmasked region, \sim 15 s of additional etching is done after observing the endpoint by a laser interferometer (LEM, HORIBA Scientific). In the same RIE machine, an Ar-plasma sputter cleaning process (20 sccm Ar flow, 10 μ bar chamber pressure, and 100 W RF power) is performed for 5 min to remove the oxidized Cr layer on the surface of the hard mask and the sacrificial layer, which is probably induced during the previous etching step. This additional step substantially enhances the wet etching process of the remnant Cr layers in the later step, as such oxidized Cr is much less dissoluble in Cr etchant solution.

To retrieve the particles, the samples are manually cleaved into 5 mm \times 5 mm chips. Each chip is firstly soaked in a Cr etchant solution (dark yellow; TechniEtch Cr01, MicroChemicals) for 10 min, where the top Cr mask and the bottom sacrificial Cr layer are dissolved altogether (**Fig. S8i**). Then, the chip is gently immersed into ample amount of DI water for 30 s for the initial washing of Cr etchant droplets (the color of DI water turns into light yellow after washing) (**Fig. S8j**), followed by the second immersion into another beaker of ample DI water for 1 min without any agitation, which completely removes all etchant from its surface (the DI water after washing remains as transparent as fresh DI water) (**Fig. S8k**). Until this second immersion into the DI beaker, the most MM particles are still staying on the surface. However, they become visibly released from the surface when the chip is very slowly taken out from the second DI beaker and passing through the water-air interface while keeping its surface facing upward, presumably due to the surface tension of water. The taken out chip and the water droplet (which is already containing many released particles) on its surface are then transferred together into a 2 mL-volume plastic tube containing fresh DI of 200 μ L, followed by vortexing of the tube for 30 s (**Fig. S8l**). The chip, whose surface is only clean Si after the vortexing, is removed from the tube and the remaining particle solution is expected to have a concentration of $\sim 2 \times 10^4$ particles per μ L, estimated from the solution volume, chip size, and the pitches of the particle array (**Fig. S10**). As the particles are directly dispersible into the water, the fraction of actually collected particles is much higher than what we have observed from our another top-down protocol without using a sacrificial layer, in which some fraction of particles are lost by contacting a sharp blade and a pipette tip [10]. By SEM inspection of the randomly dispersed MM particles on a Si substrate, the complete removal of both top Cr layer as a hard mask and bottom Cr layer as a sacrificial layer has been observed (**Fig. S10**). This observation is further confirmed by the stable 3D optical trapping of MM particles, as such trapping would not be possible due to the high scattering force if there remains any Cr layer on MM particle surface.

Measurements of linear and angular optical trapping properties

The optical trapping experiments are conducted in our home-built optical torque wrench setup. The setup schematic is shown in **Fig. S11** and more details can be found in Ref. [10]. For the sample chamber, we use a custom-made flow cell assembled with two borosilicate glass coverslips (No. 1.5H, Marienfeld) separated by a single-layer Parafilm spacer of \sim 100 μ m thickness. The flow cell channel is completely filled with the MM particle solution without any air bubble inside, and both input and output of the channel are sealed by vacuum grease (18405, Sigma-Aldrich). For all measurements, the MM particle solution is diluted until the concentration is low enough to have small probability of collision with other particles during measurements.

We measured on ten different multilayer MM particle batches (A3–5, B3–5, and C3–6), and 3–7 particles were recorded from each batch. For measurement and analysis of linear and angular trapping properties, we used our previously developed methods [54, 10]. Notably, the frequency sweep method [10] is used in the torque-speed curve measurements (**Fig. 5**).

Additional information

The Supporting Information is available at DOI: (DOI will be added here).

Author contributions

Y.T., S.H., N.H.D., and A.J.L.A designed the research. A.J.L.A. and N.H.D. directed the research. Y.T. conducted theoretical calculations, developed FEM numerical models, and fabricated MM particles from multilayer structures.

S.H. advised on the fabrication, conducted experimental measurements, and analyzed the experimental data. T.B. and J.L. deposited the multilayer structures. Y.T., S.H., H.P.U., N.H.D., and A.J.L.A. discussed the data. Y.T., S.H., N.H.D., and A.J.L.A. wrote the manuscript.

Competing financial interests

The authors declare no competing financial interest.

Acknowledgments

We thank Joseph Braat for advice on optical modeling; Daniel Tam for advice on developing numerical models for cylinder drag calculation; Marc Zuiddam, Charles de Boer, Marco van der Krogt, Hozanna Miro, Majid Ahmadi, Wiel Evers, Arnold van Run, and Anja van Langen-Suurling for technical advice on nanofabrication; Margreet Docter, Roland Dries, and Jacob Kerssemakers for technical advice on the OTW setup; Dimitri de Roos for the production of custom-made mechanical parts for the OTW setup; Theo van Laar and Sacha Khaiboulov for help with laboratory infrastructure.

This work is supported by the Faculty of Applied Sciences at Delft University of Technology (scienceDATE grant 2017; to Y.T. and S.H.); by funding provided by the China Scholarship Council under grant number 201306160089 (to Y.T.); by NanoNextNL, a micro- and nanotechnology consortium of the Government of the Netherlands and 130 partners (to N.H.D.); by the Department of Bionanoscience at Delft University of Technology (to N.H.D.); by the Foundation for Fundamental Research on Matter (FOM), part of the Netherlands Organisation for Scientific Research (NWO) (to N.H.D.); and by the European Research Council (ERC) Consolidator Grant under grant number 312221 (DynGenome; to N.H.D.).

References

- [1] Paolo Polimeno, Alessandro Magazzù, Maria Antonia Iatì, Francesco Patti, Rosalba Saija, Cristian Degli Esposti Boschi, Maria Grazia Donato, Pietro G. Gucciardi, Philip H. Jones, Giovanni Volpe, and Onofrio M. Maragò. Optical tweezers and their applications. Journal of Quantitative Spectroscopy and Radiative Transfer, 218:131–150, oct 2018.
- [2] Scott Forth, Maxim Y Sheinin, James Inman, and Michelle D Wang. Torque measurement at the single-molecule level. Annual review of biophysics, 42:583–604, 2013.
- [3] Marco Capitanio and Francesco S Pavone. Interrogating biology with force: single molecule high-resolution measurements with optical tweezers. Biophysical journal, 105(6):1293–1303, 2013.
- [4] Yoshihiko Arita, Michael Mazilu, and Kishan Dholakia. Laser-induced rotation and cooling of a trapped microgyroscope in vacuum. Nature communications, 4:2374, 2013.
- [5] Jonghoon Ahn, Zhujing Xu, Jaehoon Bang, Yu-Hao Deng, Thai M Hoang, Qinkai Han, Ren-Min Ma, and Tongcang Li. Optically Levitated Nanodumbbell Torsion Balance and GHz Nanomechanical Rotor. Physical Review Letters, 121(033603), 2018.
- [6] Fan Nan and Zijie Yan. Light-induced self-assembly: Silver-nanowire-based interferometric optical tweezers for enhanced optical trapping and binding of nanoparticles (adv. funct. mater. 7/2019). Advanced Functional Materials, 29(7):1970043, 2019.
- [7] Ian Williams, Erdal C. Oğuz, Thomas Speck, Paul Bartlett, Hartmut Löwen, and C. Patrick Royall. Transmission of torque at the nanoscale. Nature Physics, 12(1):98–103, jan 2016.
- [8] Lei Shao, Zhong-Jian Yang, Daniel Andren, Peter Johansson, and Mikael Käll. Gold nanorod rotary motors driven by resonant light scattering. ACS nano, 9(12):12542–12551, 2015.
- [9] Lei Shao and Mikael Käll. Light-Driven Rotation of Plasmonic Nanomotors. Advanced Functional Materials, 28(25):1706272, jun 2018.

- [10] Seungkyu Ha, Ying Tang, Maarten M van Oene, Richard Janissen, Roland M Dries, Belen Solano, Aurèle JL Adam, and Nynke H Dekker. Single-crystal rutile tio₂ nanocylinders are highly effective transducers of optical force and torque. ACS photonics, 2019.
- [11] Christopher Deufel, Scott Forth, Chad R Simmons, Siavash Dejgosha, and Michelle D Wang. Nanofabricated quartz cylinders for angular trapping: Dna supercoiling torque detection. Nature methods, 4(3):223, 2007.
- [12] Zhuangxiong Huang, Francesco Pedaci, Maarten Van Oene, Matthew J Wiggin, and Nynke H Dekker. Electron Beam Fabrication of Birefringent Microcylinders. ACS Nano, 2011.
- [13] Ping-Chun Li, Jen-Chien Chang, Arthur La Porta, and T Yu Edward. Fabrication of birefringent nanocylinders for single-molecule force and torque measurement. Nanotechnology, 25(23):235304, 2014.
- [14] M. E. J. Friese, T. A. Nieminen, N. R. Heckenberg, and H. Rubinsztein-Dunlop. Optical alignment and spinning of laser-trapped microscopic particles. Nature, 394(6691):348–350, jul 1998.
- [15] Yoshihiko Arita, Joseph M Richards, Michael Mazilu, Gabriel C Spalding, Susan E Skelton Spesyvtseva, Derek Craig, and Kishan Dholakia. Rotational dynamics and heating of trapped nanovaterite particles. ACS nano, 10(12):11505–11510, 2016.
- [16] Avin Ramaiya, Basudev Roy, Michael Bugiel, and Erik Schäffer. Kinesin rotates unidirectionally and generates torque while walking on microtubules. Proceedings of the National Academy of Sciences, 114(41):10894–10899, 2017.
- [17] Carlo Liberale, Paolo Minzioni, Francesca Bragheri, Francesco De Angelis, Enzo Di Fabrizio, and Ilaria Cristiani. Miniaturized all-fibre probe for three-dimensional optical trapping and manipulation. Nature photonics, 1(12):723, 2007.
- [18] S Stallinga. Optical trapping at low numerical aperture. Journal of the European Optical Society-Rapid Publications, 6, 2011.
- [19] Edwin En-Te Hwu and Anja Boisen. Hacking cd/dvd/blu-ray for biosensing. ACS sensors, 3(7):1222–1232, 2018.
- [20] Steven L Neale, Michael P MacDonald, Kishan Dholakia, and Thomas F Krauss. All-optical control of microfluidic components using form birefringence. Nature Materials, 4(7):530–533, 2005.
- [21] E Higurashi, Renshi Sawada, and T Ito. Optically induced angular alignment of birefringent micro-objects by linear polarization. Applied physics letters, 73(21):3034–3036, 1998.
- [22] Lars Friedrich and Alexander Rohrbach. Surface imaging beyond the diffraction limit with optically trapped spheres. Nature nanotechnology, 10(12):1064, 2015.
- [23] Willie J Padilla, Dimitri N Basov, and David R Smith. Negative refractive index metamaterials. Materials today, 9(7-8):28–35, 2006.
- [24] Muhan Choi, Seung Hoon Lee, Yushin Kim, Seung Beom Kang, Jonghwa Shin, Min Hwan Kwak, Kwang-Young Kang, Yong-Hee Lee, Namkyoo Park, and Bumki Min. A terahertz metamaterial with unnaturally high refractive index. Nature, 470(7334):369, 2011.
- [25] Li Min, Li-Rong Huang, Rong Sun, Man-Man Xi, and Zhi-Wei Li. Dual metamaterial with large birefringence. IEEE Photonics Journal, 7(6):1–8, 2015.
- [26] Meng Chen, Fei Fan, Shi-Tong Xu, and Sheng-Jiang Chang. Artificial high birefringence in all-dielectric gradient grating for broadband terahertz waves. Scientific reports, 6:38562, 2016.
- [27] Yu Guo, Ward Newman, Cristian L. Cortes, and Zubin Jacob. Applications of hyperbolic metamaterial substrates. Advances in OptoElectronics, 2012(1):1–10, 2012.
- [28] Rong-Chung Tyan, Atul A Salvekar, Hou-Pu Chou, Chuan-Cheng Cheng, Axel Scherer, Pang-Chen Sun, Fang Xu, and Yeshayahu Fainman. Design, fabrication, and characterization of form-birefringent multilayer polarizing beam splitter. JOSA A, 14(7):1627–1636, 1997.

- [29] S. Lang, H. S. Lee, A. Yu Petrov, M. Störmer, M. Ritter, and M. Eich. Gold-silicon metamaterial with hyperbolic transition in near infrared. Applied Physics Letters, 103(2):1–5, 2013.
- [30] Sergey S. Kruk, Zi Jing Wong, Ekaterina Pshenay-Severin, Kevin O’Brien, Dragomir N. Neshev, Yuri S. Kivshar, and Xiang Zhang. Magnetic hyperbolic optical metamaterials. Nature Communications, 7:11329, 2016.
- [31] Jingbo Sun, Mikhail I. Shalaev, and Natalia M. Litchinitser. Experimental demonstration of a non-resonant hyperlens in the visible spectral range. Nature Communications, 6(May):7201, 2015.
- [32] Ryan Badman, Fan Ye, Wagma Caravan, and Michelle D Wang. High trap stiffness microcylinders for nanophotonic trapping. ACS Applied Materials & Interfaces, 2019.
- [33] Vito Clericò, Luca Masini, Adriano Boni, Sandro Meucci, Marco Cecchini, Fabio A Recchia, Alessandro Tredicucci, and Angelo Bifone. Water-dispersible three-dimensional lc-nanoresonators. PloS one, 9(8):e105474, 2014.
- [34] Wenshan Cai and Vladimir M Shalaev. Optical metamaterials, volume 10. Springer, 2010.
- [35] O El Gawhary, MC Dheur, SF Pereira, and JJM Braat. Extension of the classical fabry–perot formula to 1d multilayered structures. Applied Physics B, 111(4):637–645, 2013.
- [36] Julien Lumeau, Fabien Lemarchand, Thomas Begou, Detlef Arhilger, and Harro Hagedorn. Angularly tunable bandpass filter: design, fabrication, and characterization. Optics letters, 44(7):1829–1832, 2019.
- [37] Sidharam P Pujari, Luc Scheres, Antonius TM Marcelis, and Han Zuilhof. Covalent surface modification of oxide surfaces. Angewandte Chemie International Edition, 53(25):6322–6356, 2014.
- [38] Lihong Gao, Fabien Lemarchand, and Michel Lequime. Exploitation of multiple incidences spectrometric measurements for thin film reverse engineering. Optics express, 20(14):15734–15751, 2012.
- [39] Swagato Sarkar, Vaibhav Gupta, Mohit Kumar, Jonas Schubert, Patrick T Probst, Joby Joseph, and Tobias AF König. Hybridized guided-mode resonances via colloidal plasmonic self-assembled grating. ACS applied materials & interfaces, 11(14):13752–13760, 2019.
- [40] Thomas Siefke, Stefanie Kroker, Kristin Pfeiffer, Oliver Puffky, Kay Dietrich, Daniel Franta, Ivan Ohlídal, Adriana Szeghalmi, Ernst-Bernhard Kley, and Andreas Tünnermann. Materials pushing the application limits of wire grid polarizers further into the deep ultraviolet spectral range. Advanced Optical Materials, 4(11):1780–1786, 2016.
- [41] Rémi Boidin, Tomáš Halenkovič, Virginie Nazabal, Ludvík Beneš, and Petr Němec. Pulsed laser deposited alumina thin films. Ceramics International, 42(1):1177–1182, 2016.
- [42] Darwin L Wood, Kurt Nassau, TY Kometani, and DL Nash. Optical properties of cubic hafnia stabilized with yttria. Applied optics, 29(4):604–607, 1990.
- [43] Braulio Gutiérrez-Medina, Johan OL Andreasson, William J Greenleaf, Arthur LaPorta, and Steven M Block. An optical apparatus for rotation and trapping. In Methods in enzymology, volume 475, pages 377–404. Elsevier, 2010.
- [44] Francesco Pedaci, Zhuangxiong Huang, Maarten Van Oene, Stephane Barland, and Nynke H Dekker. Excitable particles in an optical torque wrench. Nature Physics, 7(3):259, 2011.
- [45] Murat Muradoglu and Tuck Wah Ng. Optical trapping map of dielectric spheres. Applied optics, 52(15):3500–9, 2013.
- [46] Alexander Rohrbach. Stiffness of optical traps: quantitative agreement between experiment and electromagnetic theory. Physical review letters, 95(16):168102, 2005.
- [47] Ashley L Nord, Emilie Gachon, Ruben Perez-Carrasco, Jasmine A Nirody, Alessandro Barducci, Richard M Berry, and Francesco Pedaci. Catch bond drives stator mechanosensitivity in the bacterial flagellar motor. Proceedings of the National Academy of Sciences, 114(49):12952–12957, 2017.

- [48] SH Simpson. Inhomogeneous and anisotropic particles in optical traps: Physical behaviour and applications. Journal of Quantitative Spectroscopy and Radiative Transfer, 146:81–99, 2014.
- [49] Seungkyu Ha, Richard Janissen, Yera Ye Ussembayev, Maarten M van Oene, Belen Solano, and Nynke H Dekker. Tunable top-down fabrication and functional surface coating of single-crystal titanium dioxide nanostructures and nanoparticles. Nanoscale, 8(20):10739–10748, 2016.
- [50] Maarten M. van Oene, Seungkyu Ha, Tessa Jager, Mina Lee, Francesco Pedaci, Jan Lipfert, and Nynke H. Dekker. Quantifying the Precision of Single-Molecule Torque and Twist Measurements Using Allan Variance. Biophysical Journal, 114(8):1970–1979, apr 2018.
- [51] B Richards and E Wolf. Electromagnetic diffraction in optical systems, ii. structure of the image field in an aplanatic system. Proc. R. Soc. Lond. A, 253(1274):358–379, 1959.
- [52] Emil Wolf. Electromagnetic diffraction in optical systems-i. an integral representation of the image field. Proc. R. Soc. Lond. A, 253(1274):349–357, 1959.
- [53] Jun Chen, Jack Ng, Zhifang Lin, and C. T. Chan. Optical pulling force. Nature Photonics, 5(9):531–534, 2011.
- [54] Francesco Pedaci, Zhuangxiong Huang, Maarten van Oene, and Nynke H. Dekker. Calibration of the optical torque wrench. Optics Express, 20(4):3787, feb 2012.
- [55] Zhanna Santybayeva and Francesco Pedaci. Optical torque wrench design and calibration. In Methods in Molecular Biology, volume 1486, pages 157–181. Humana Press, New York, NY, 2017.
- [56] Frederick Gittes and Christoph F Schmidt. Interference model for back-focal-plane displacement detection in optical tweezers. Optics letters, 23(1):7–9, 1998.

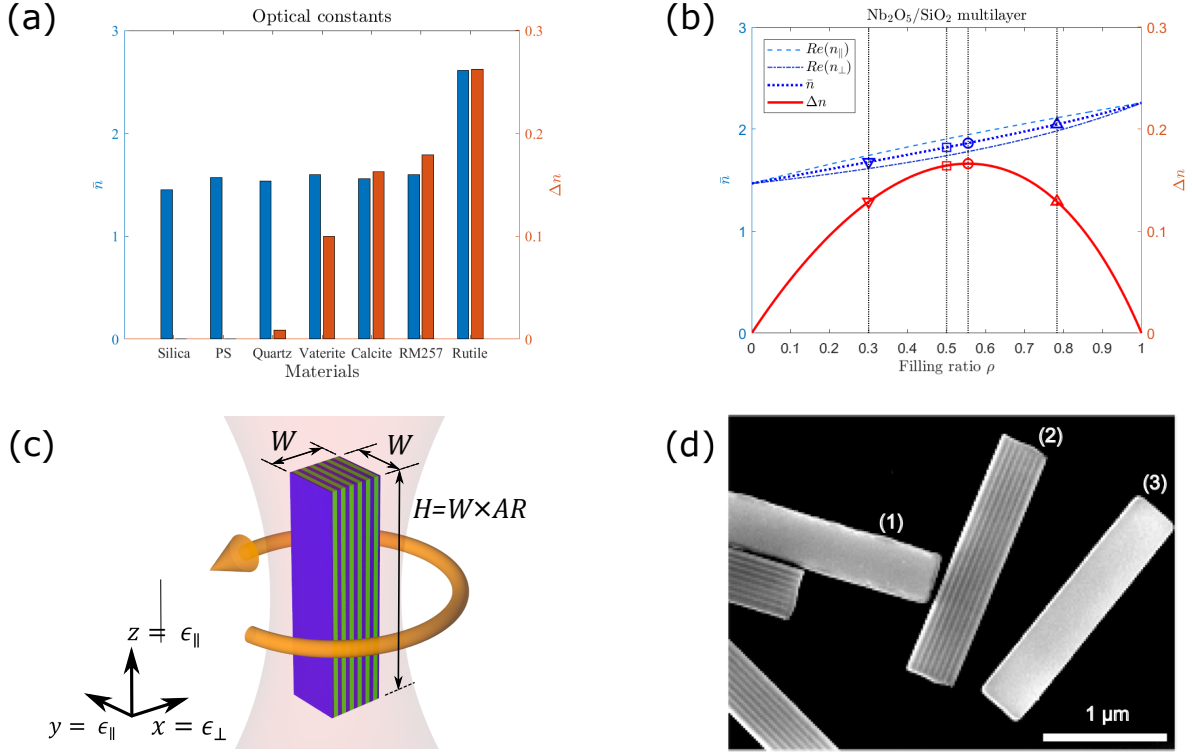


Figure 1: The design principles of the multilayer MM particles. (a) The optical constants of the most common materials for optical trapping (silica, polystyrene (PS), Quartz SiO₂, Vaterite CaCO₃, Calcite CaCO₃, RM257 liquid crystal, and Rutile TiO₂, from left to right columns). For each material, the average refractive index (blue left-side bar with its value at left y -axis) and optical birefringence (red right-side bar with its value at right y -axis) are shown. (b) The EMT-predicted effective indices and birefringence of Nb₂O₅/SiO₂ multilayer structure, as a function of material filling ratio ρ . The calculated n_{\parallel} (light blue dashed line) and n_{\perp} (dark blue dash-dotted line) of the multilayer are shown, together with the resulting \bar{n} ($= (n_{\parallel} + n_{\perp})/2$; blue dotted line) and Δn ($= |n_{\parallel} - n_{\perp}|$; red line). The filling ratios of our interest and the corresponding optical constants are indicated by the black dotted vertical lines and the corresponding symbols overlaid on the lines, respectively. Our fabricated samples have either $\rho = 0.3$ (downward triangles; wafer A and B) or $\rho = 0.5$ (squares; wafer C), while the maximum birefringence occurs at $\rho = 0.55$ (circles). Except the maximum, the same birefringence can be achieved at two different filling ratios. For example, the birefringence of the multilayer with $\rho = 0.3$ can be obtained with $\rho = 0.78$ (upward triangles) as well. (c) A schematic of an optically trapped multilayer MM square cuboid particle made of Nb₂O₅ (green) and SiO₂ (blue), at the focus of the laser beam (red). The optic axis (x -axis) of the particle is normal to the multilayer interfaces (i.e., y - z plane), exhibiting the refractive index n_{\perp} which is lower than those along y - and z -axis (n_{\parallel}). The cross section along the x - y plane is a square of width W , and the aspect ratio AR determines height H along the z -axis. The direction of particle rotation (an orange curved arrow) is shown, which is possible by means of the modulation of the input beam linear polarization. (d) A scanning electron microscopy (SEM) image of fabricated multilayer MM particles with $\rho = 0.3$, $W = 400$ nm, and $AR = 5$. The differently oriented particles allow to observe the top (1), side (2), and bottom (3) of the particles. In particular, the side (2) shows the multilayer structure in which Nb₂O₅ (brighter region) and SiO₂ (darker region) layers can be clearly distinguished. Also, the top (1) (on which Cr hard etch mask was located) shows rough edges due to the damage during dry etching, while the bottom (3) (which was facing sacrificial Cr layer) has smooth edges.

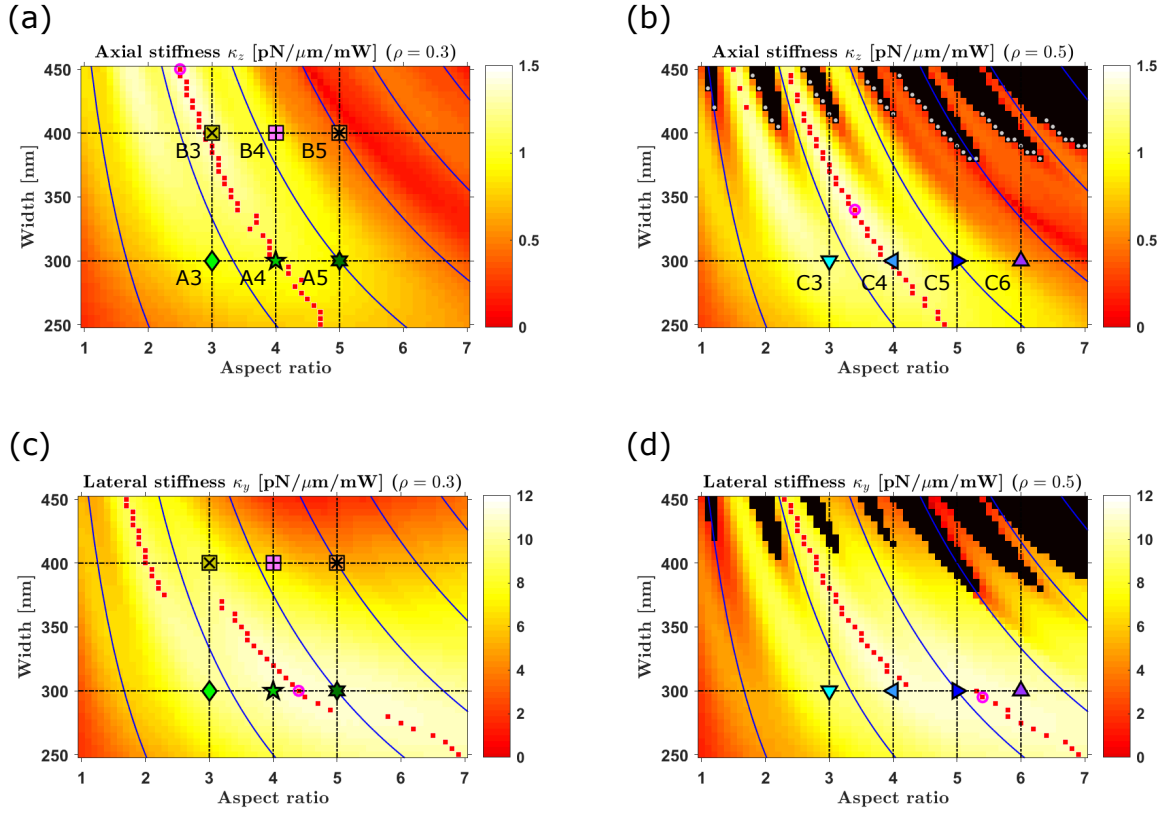


Figure 2: The numerically (FEM) calculated maps for the linear trapping stiffnesses of multilayer MM nano-cuboids. The axial stiffness (κ_z) (a,b) and the lateral stiffness (κ_y) (c,d) are shown as a function of aspect ratio AR and width W of the nano-cuboids, for material filling ratios of $\rho = 0.3$ (a,c) and $\rho = 0.5$ (b,d). The pixel size of each map is set as $\Delta AR = 0.1$ and $\Delta W = 5$ nm. The solid blue lines represent the equal heights of the nano-cuboids with the interval of 500 nm, from 500 nm (leftmost) to 3000 nm (rightmost). As a visual guidance for finding the particle dimensions that maximize linear stiffnesses, the particle dimensions for the local maxima per each width W is displayed by the overlaid red squares, while the optimal particle dimension for the maximum of each map is additionally marked by the overlaid magenta circle in panels (a–d). The dimensions of the designed particle batches for fabrication are displayed by the cross-points (overlaid with the corresponding symbols) of the horizontal and vertical black dash-dotted lines. The labels of the entire ten particle batches (from A3 to C6) are shown in panels (a,b). The black pixels in the maps of $\rho = 0.5$ (b,d) indicate the particle dimensions that cannot be trapped in 3D due to the dominant scattering forces. The minimum diameter that results in a black pixel for each AR (i.e., the calculated 3D-trappability threshold diameter) is shown as a gray dot in panel (b).

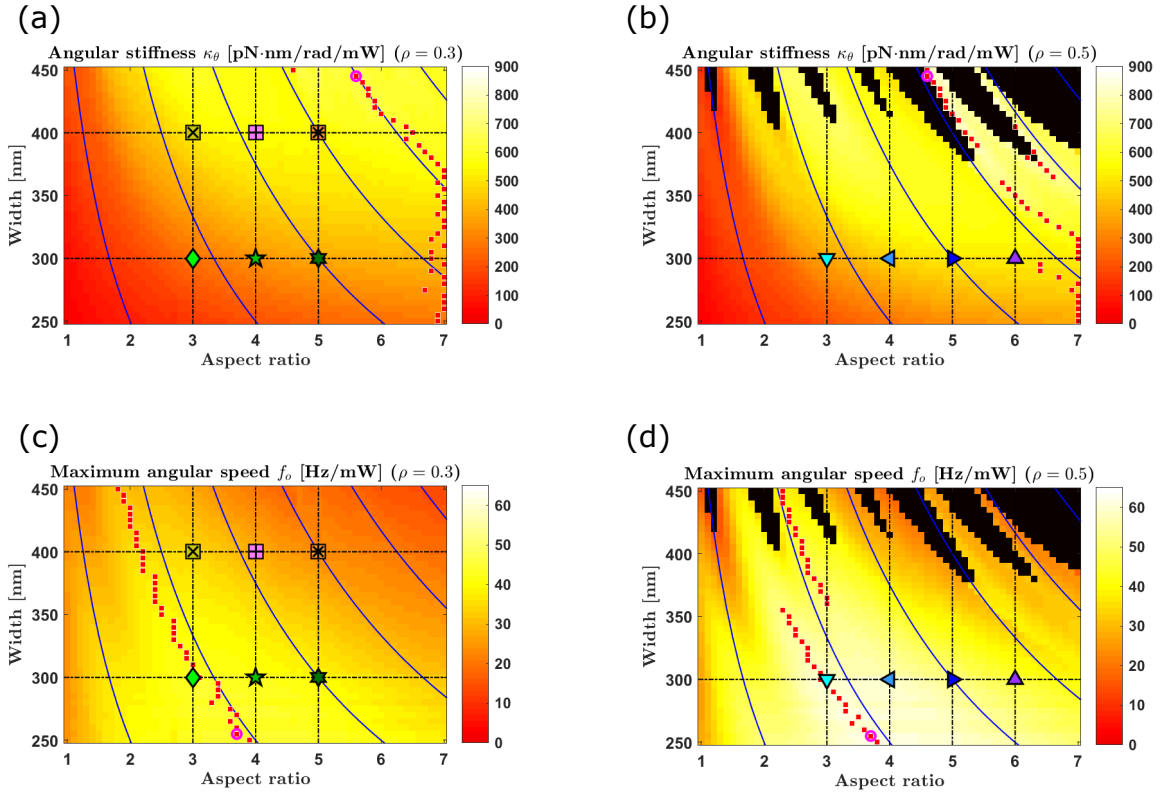


Figure 3: The numerically (FEM) calculated maps for the angular trapping properties of multilayer MM nano-cuboids. The angular stiffness (κ_θ) (a,b) and the maximum angular speed (f_o) (c,d) are shown as a function of aspect ratio AR and width W of the nano-cuboids, for material filling ratios of $\rho = 0.3$ (a,c) and $\rho = 0.5$ (b,d). The pixel size of each map is set as $\Delta AR = 0.1$ and $\Delta W = 5$ nm. The solid blue lines represent the equal heights of the nano-cuboids with the interval of 500 nm, from 500 nm (leftmost) to 3000 nm (rightmost). As a visual guidance for finding the particle dimensions that maximize angular stiffness and angular rotation frequency, the particle dimensions for the local maxima per each width W is displayed by the overlaid red squares, while the optimal particle dimension for the maximum of each map is additionally marked by the overlaid magenta circle in panels (a–d). The dimensions of the designed particle batches for fabrication are displayed by the cross-points (overlaid with the corresponding symbols; the same shape and color coding as shown in **Fig. 2**) of the horizontal and vertical black dash-dotted lines. The black pixels in the maps of $\rho = 0.5$ (b,d) indicate the particle dimensions that cannot be trapped in 3D.

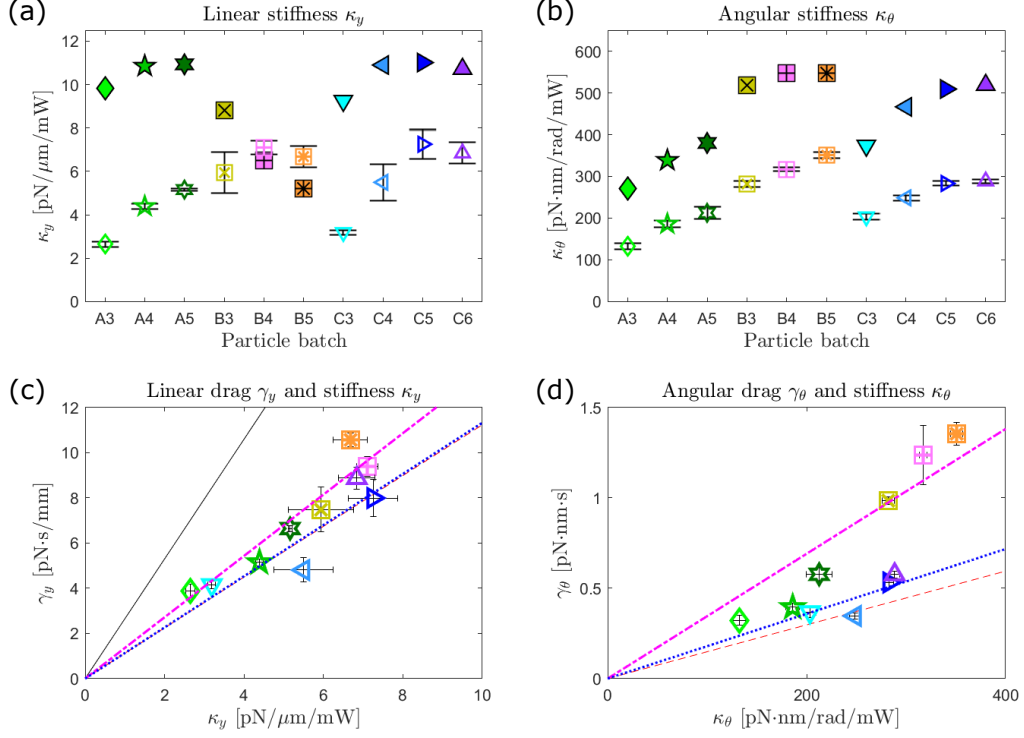


Figure 4: The OTW-measured linear and angular trapping properties of multilayer MM nano-cuboids. For the entire ten batches of nano-cuboids (from A3 to C6), the measurement results of the linear stiffness κ_y (a) and the angular stiffness κ_θ (b) are shown (empty symbols and errorbars denote the mean and the standard deviation (mean \pm S.D.) of each batch, respectively), together with the corresponding FEM-predicted values (filled symbols). The same measured linear and angular stiffness values (κ) are plotted once more with the corresponding drag coefficients (γ) (the same representation of symbols and errorbars as shown in panels (a,b)), revealing the characteristic response times ($t_c = \gamma/\kappa$) (c,d). The representative response time for each material filling ratio ρ has been found as the slope of the linear fit (forced through the origin) to the corresponding data points of the particles with the same ρ (magenta dash-dotted line for $\rho = 0.3$; blue dotted line for $\rho = 0.5$). For comparison, the linear fit to the data points (which have been measured in the same setup and conditions [10]) of PS beads (black line; for linear data only in panel (c)) and rutile TiO_2 particles (red dashed line; for both linear and angular data in panels (c,d)) are overlaid. The data values shown in all panels (a–d) are summarized in **Table. S2**.

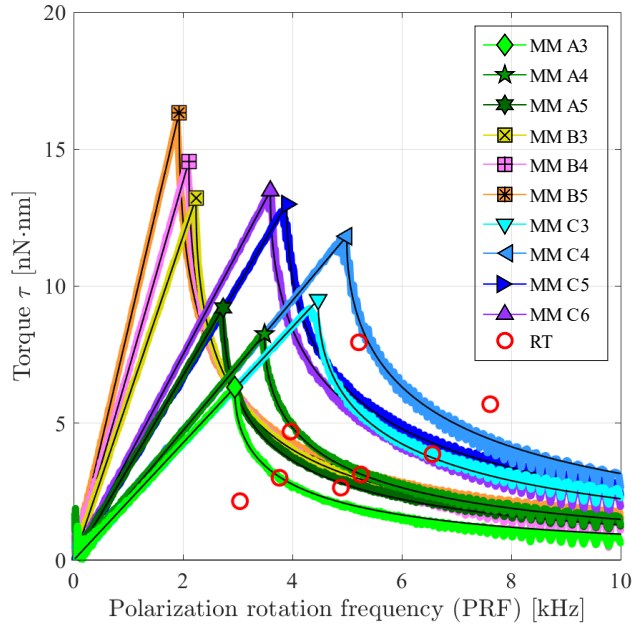


Figure 5: The measured optical torque of multilayer MM nano-cuboids as a function of input beam polarization rotation frequency (PRF). The entire ten batches (from A3 to C6) are measured in water at the laser beam power of 92 mW. Each colored curve represents the moving-averaged torque of a single MM nano-cuboid selected from each batch. Its fitting result to the theoretical equation [55] is overlaid as a black line and its maximum torque-speed data point is marked by the corresponding symbol (see legend; the same shape and color coding as shown in **Fig. 2**). From zero PRF to the PRF that results in the maximum torque, PRF is identical to the rotation frequency (f) of the trapped particle to which the optical torque (τ) is directly proportional, with angular drag (γ_θ) as the proportionality constant ($\tau = 2\pi\gamma_\theta f$). Additionally, the data points measured from rutile TiO_2 (RT) nanocylinders [10] (red circles) are shown together for comparison. The small spikes near zero PRF and the ripples at higher PRF are attributed to the artifacts of the measurement method [10].

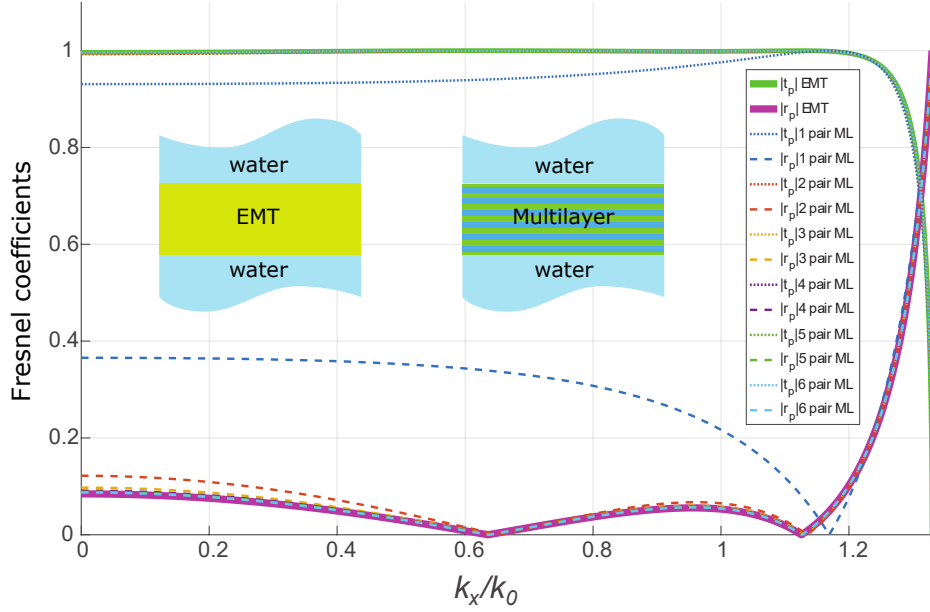


Figure S1: The magnitude of the Fresnel coefficients ($|t_p|$ and $|r_p|$) as a function of transversal wavenumber k_x/k_0 , calculated for a $\text{Nb}_2\text{O}_5/\text{SiO}_2$ multilayer (ML) and its equivalent single layer (SL) structure (whose effective optical constants are predicted by the effective medium theory (EMT)). For a ML structure with any layer-pair number N , in order to have a symmetric structure, we put SiO_2 as the first and the last layers (each of them has half-thickness compared to that of single SiO_2 layer in the middle of the ML stack). In the calculations using our custom Matlab code (according to Ref. [35]), for both model structures, we set the surrounding medium as water, the total thickness of each structure as 300 nm, and the vacuum wavelength of the incident beam as 1064 nm. The inset graphic shows the schematics of the SL model (at left) and the six layer-pair ML model (at right). This result shows that, as long as the layer-pair number N is large enough, the EMT can describe the optical response of the ML stacks with high accuracy. For example, for the ML with 5–6 layer-pairs, the largest deviation from the EMT prediction is less than 0.4%.

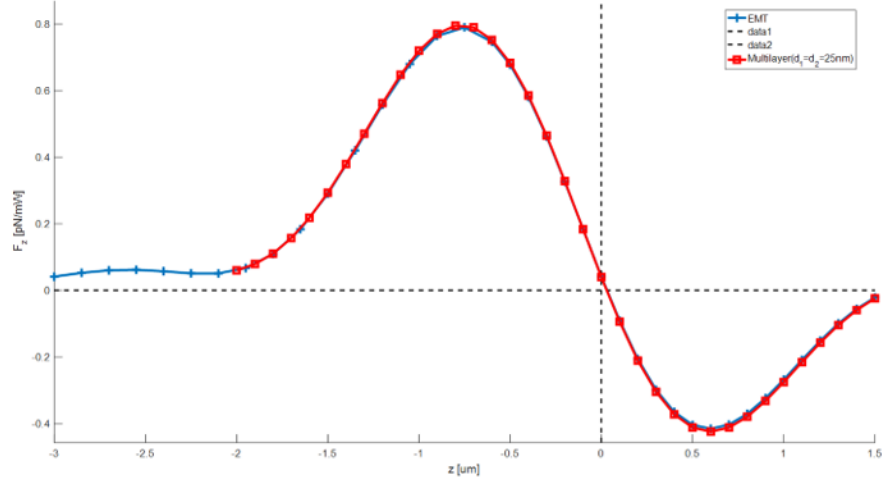


Figure S2: The finite element method (FEM) modeling results of optical force F_z along the z -axis for an optically trapped multilayer (ML; red squares connected by red lines) nano-cuboid and its equivalent single-layer (SL; blue crosses connected by blue lines) nano-cuboid (whose effective optical constants are predicted by the EMT). The width and height of each particle are set as 300 nm and 1200 nm, respectively ($AR = 4$). The ML particle is made of a $\text{Ni}_2\text{O}_5/\text{SiO}_2$ ML with a filling ratio of 0.5, while the thickness of each individual layer is 25 nm (except the first and the last SiO_2 layer which is 12.5 nm-thick). The magnitude of optical force calculated from the ML model is almost the same as that from the SL model, which validates the use of the SL model in the FEM-calculations of optical trap stiffness maps (**Fig. 2,3**).

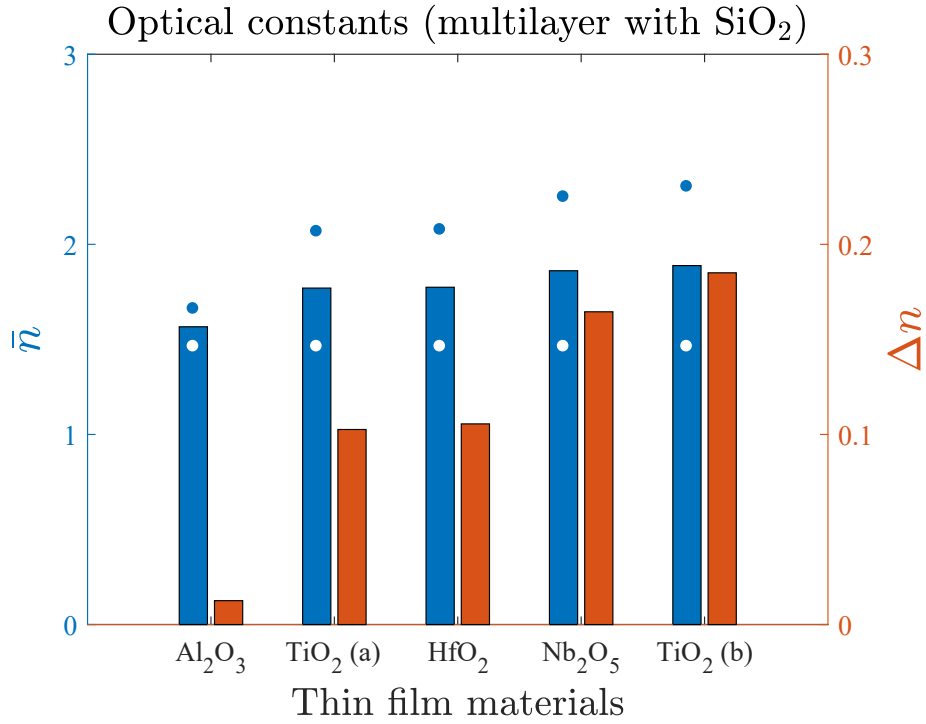


Figure S3: The possible multilayer compositions and their resulting optical constants predicted by the EMT, using combinations of diverse high-index oxide thin films (Al₂O₃ [41], TiO₂(a) [39], TiO₂(b) [40], HfO₂ [42], or Nb₂O₅ [38]; blue dots for left y -axis) with a low-index oxide thin film (SiO₂ [38]; white dots for left y -axis). For each combination, the maximum birefringence (red bar for right y -axis) and the corresponding effective refractive index (blue bar for left y -axis) are shown. For all thin films, the index values at the wavelength of 1064 nm are used for these calculations. Notably, the index of a thin film material can vary and different from that of the same material in the bulk crystalline form, depending on the employed deposition method and conditions. For example, the thin films of TiO₂(a) and TiO₂(b) are deposited by evaporation and ALD, respectively.

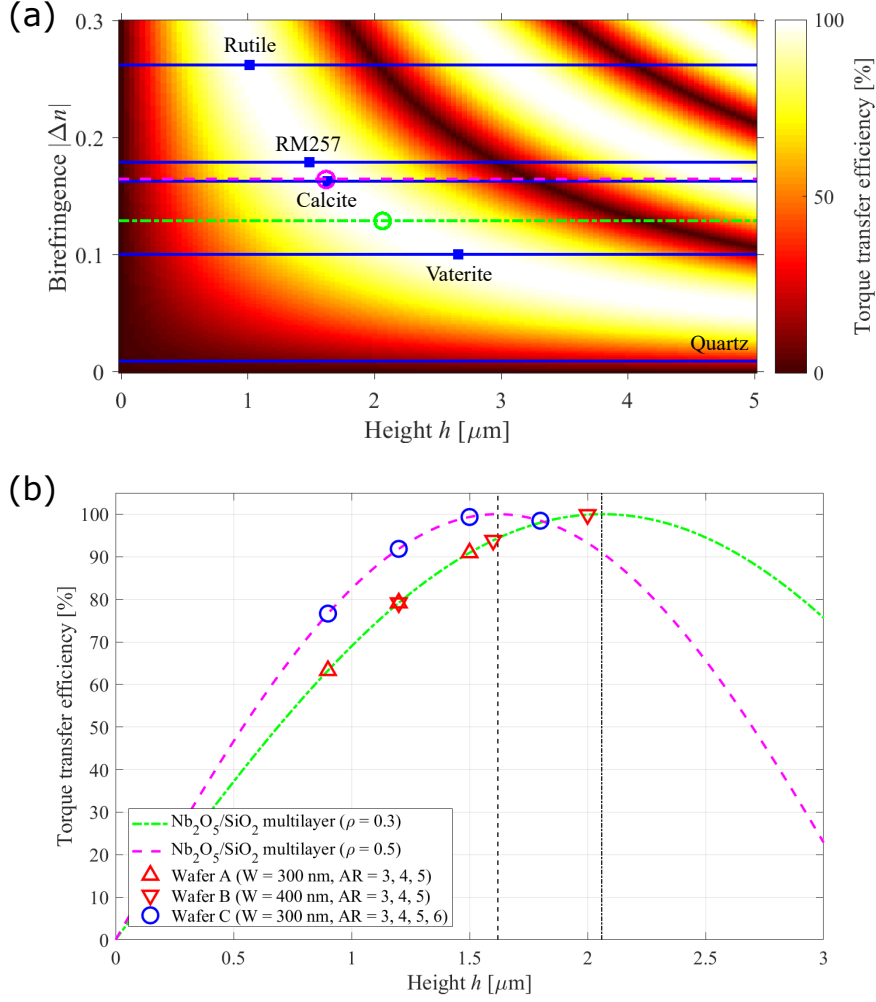


Figure S4: The predicted torque transfer efficiency (TTE) of Nb₂O₅/SiO₂ multilayer structures using the ideal equation [10] and its comparison with those of other dielectric birefringent materials. (a) Two-dimensional map of torque transfer efficiency, as a function of particle height h and birefringence $|\Delta n|$. The Nb₂O₅/SiO₂ multilayer structures with material filling ratios of $\rho = 0.3$ (green dash-dotted horizontal line for $|\Delta n|$, green circle for the maximum TTE) and $\rho = 0.5$ (magenta dashed horizontal line for $|\Delta n|$, magenta circle for the maximum TTE) are overlaid with other conventional birefringent materials (rutile TiO₂, liquid crystal RM257, calcite CaCO₃, vaterite CaCO₃, and quartz SiO₂; blue horizontal lines for $|\Delta n|$, blue squares for the maximum TTE). For quartz, the optimal height ($\sim 30 \mu\text{m}$) for the maximum TTE is outside of the displayed range of the map. Notably, the birefringence of Nb₂O₅/SiO₂ multilayer with $\rho = 0.5$ is almost identical to that of calcite. The pixel size of the map is set as 25 nm and 0.0025 for particle height and birefringence, respectively. (b) Comparison of torque transfer efficiency curves as a function of particle height, for Nb₂O₅/SiO₂ multilayer structures with material filling ratios of $\rho = 0.3$ (green dash-dotted line) and $\rho = 0.5$ (magenta dashed line). The particle heights of the fabricated ten nano-cuboid batches are marked as the corresponding symbols (red upward triangles for A3–5, red downward triangles for B3–5, and blue circles for C3–6). In particular, the nano-cuboid batch B5 ($W = 400 \text{ nm}$, $AR = 5$) and batch C5 ($W = 300 \text{ nm}$, $AR = 5$) have particle heights which result in $\sim 100\%$ torque transfer efficiency for material filling ratio $\rho = 0.3$ and $\rho = 0.5$, respectively.

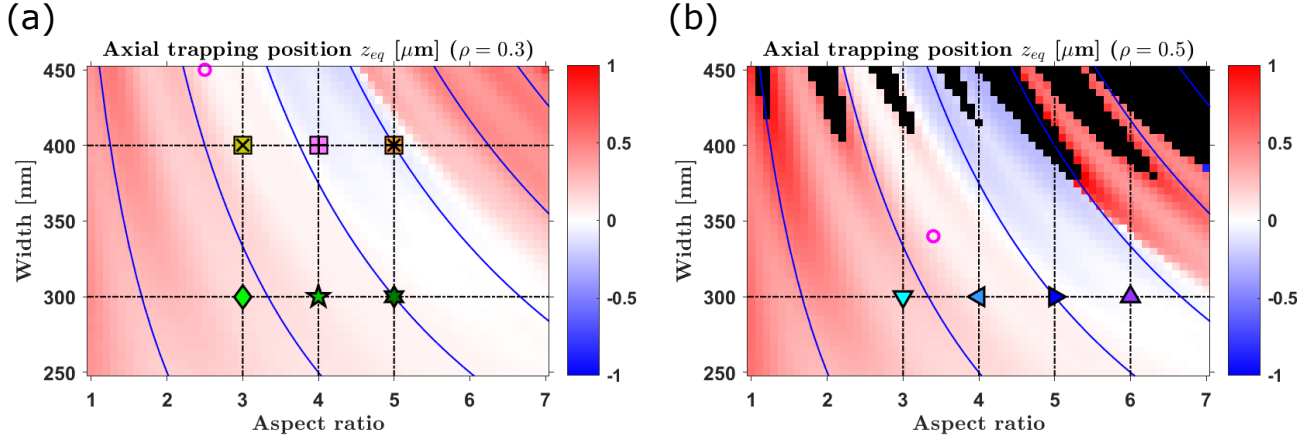


Figure S5: The equilibrium axial trapping position z_{eq} maps, for material filling ratios of (a) $\rho = 0.3$ and (b) $\rho = 0.5$. The optimal particle dimension for the maximum axial stiffness of each map (the same as shown in **Fig. 2a,b**) is additionally marked by the overlaid magenta circle in panels (a,b), showing that the axial stiffness is maximized at $z_{eq} \approx 0$ ($z_{eq} = 0.074 \mu\text{m}$ for $\rho = 0.3$; $z_{eq} = 0.083 \mu\text{m}$ for $\rho = 0.5$). The solid blue lines represent the equal heights of the nano-cuboids with the interval of 500 nm, from 500 nm (leftmost) to 3000 nm (rightmost). The dimensions of the designed particle batches (A3–5, B3–5, and C3–6) for fabrication are displayed by the cross-points (overlaid with the corresponding symbols; the same shape and color coding as shown in **Fig. 2**) of the horizontal and vertical black dash-dotted lines. The black pixels in the map of $\rho = 0.5$ (b) indicate the particle dimensions that cannot be trapped in 3D. The pixel size of each map is set as $\Delta AR = 0.1$ and $\Delta W = 5 \text{ nm}$.

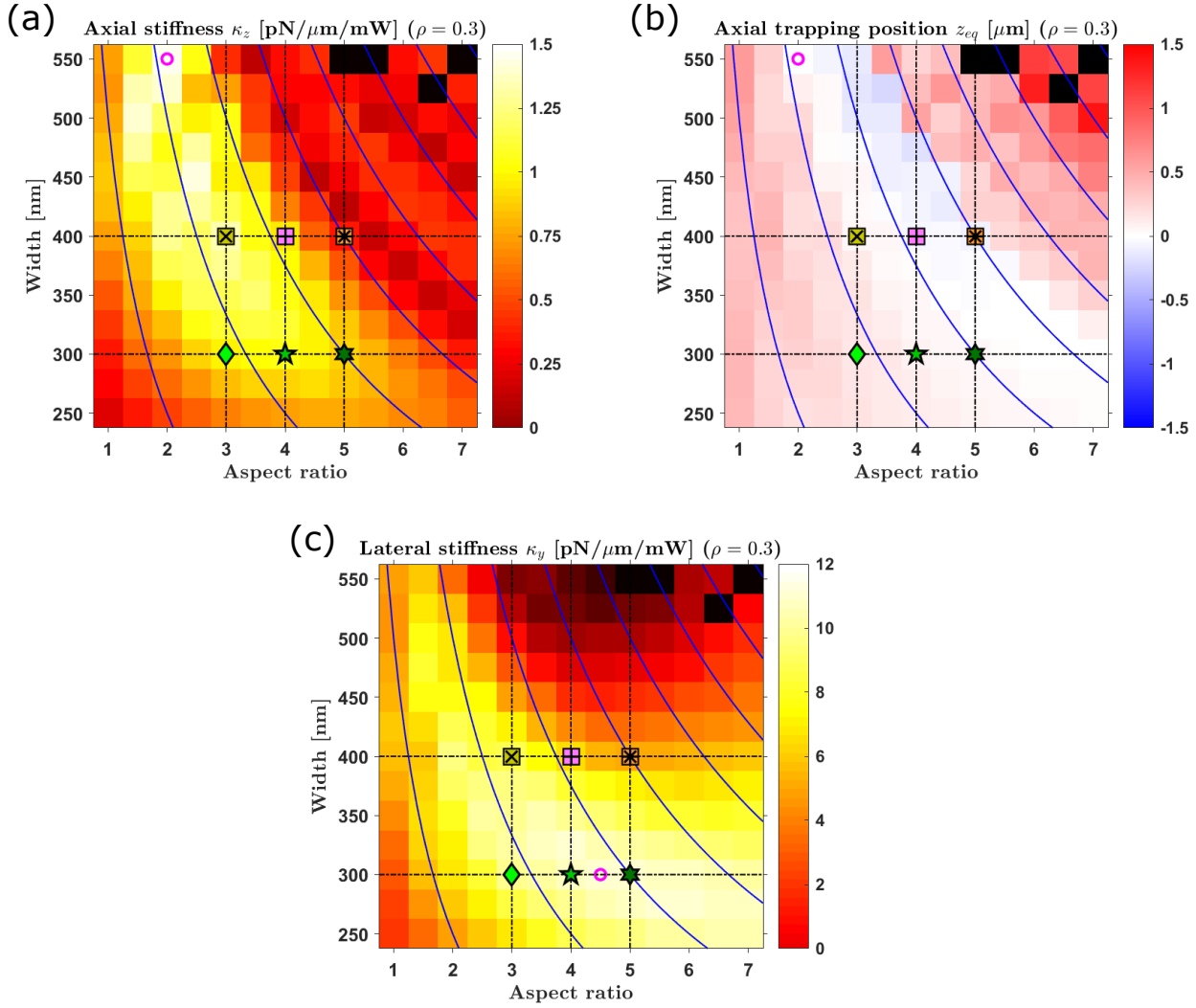


Figure S6: The linear trapping maps for the multilayer MM nano-cuboids with the smaller material filling ratio $\rho = 0.3$, extended for the larger particle widths (W up to 550 nm). The maps of (a) axial stiffness κ_z , (b) equilibrium axial trapping position z_{eq} , and (c) lateral stiffness κ_y are shown. The optimal particle dimensions for the maximum axial and lateral stiffnesses are displayed by the overlaid magenta circles in panels (a,c). The particle dimension for the maximum axial stiffness (the same as shown in panel (a)) is displayed by the overlaid magenta circle in panel (b), showing that the axial stiffness is maximized at $z_{eq} \approx 0$ ($z_{eq} = 0.081 \mu\text{m}$, precisely). The solid blue lines represent the equal heights of the nano-cuboids with the interval of 500 nm, from 500 nm (leftmost) to 3500 nm (rightmost). The dimensions of the designed particle batches (A3–5, B3–5) for fabrication are displayed by the cross-points (overlaid with the corresponding symbols; the same shape and color coding as shown in Fig. 2) of the horizontal and vertical black dash-dotted lines. The black pixels in the maps indicate the particle dimensions that cannot be trapped in 3D. The pixel size of each map is set as $\Delta AR = 0.5$ and $\Delta W = 25$ nm.

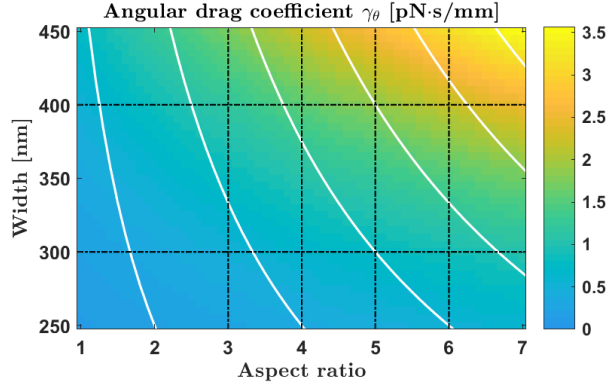


Figure S7: The FEM-calculated rotational hydrodynamic drag coefficient γ_θ map of multilayer MM nanocuboids in water, as a function of particle aspect ratio AR and width W . Together with the FEM-calculated angular stiffness κ_θ map (**Fig. 3a,b**), this rotational drag γ_θ map is used to calculate the maximum rotation frequency $f_o (= \kappa_\theta / (4\pi\gamma_\theta))$ map (**Fig. 3c,d**). The dimensions of the designed particle batches (A3–5, B3–5, and C3–6) for fabrication are displayed by the cross-points of the horizontal and vertical black dash-dotted lines. The solid white lines represent the equal heights of the nano-cuboids with the interval of 500 nm, from 500 nm (leftmost) to 3000 nm (rightmost). The pixel size of the map is set as $\Delta AR = 0.1$ and $\Delta W = 5$ nm.

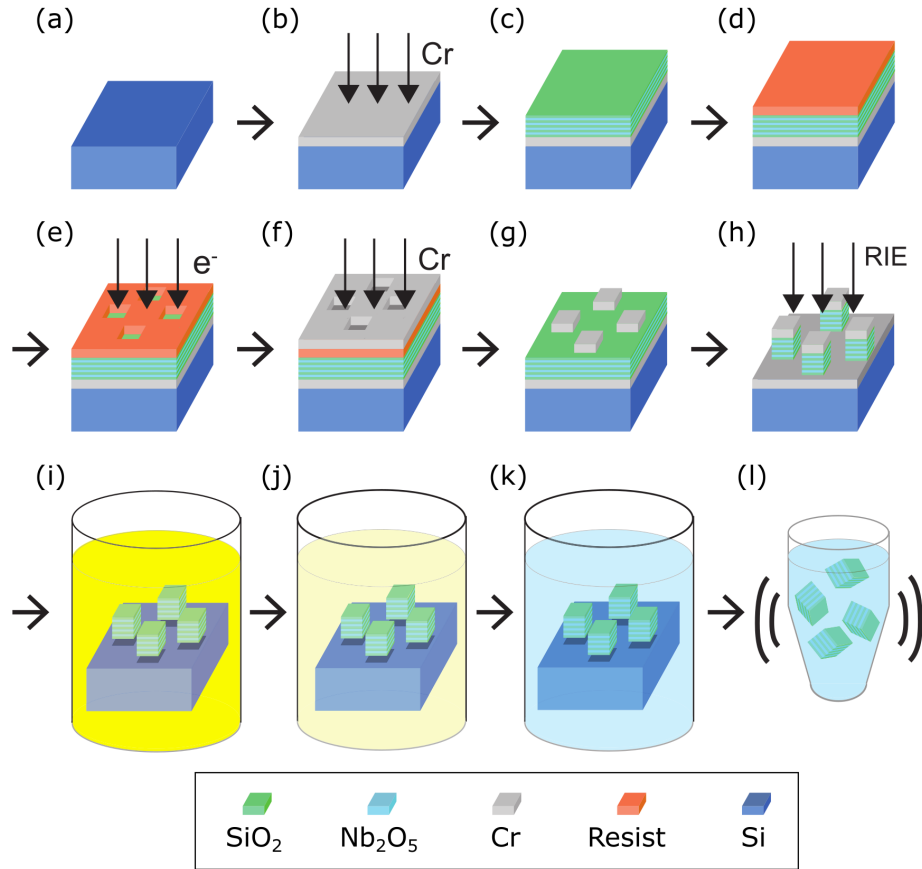
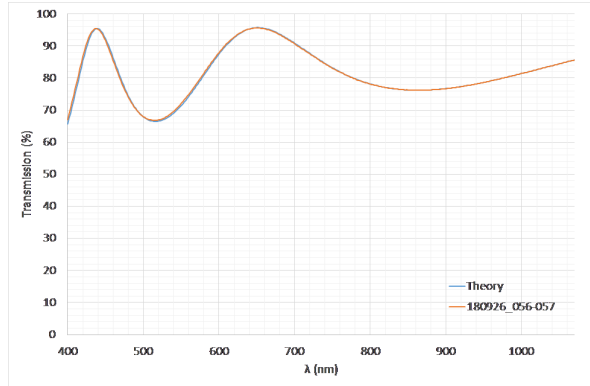
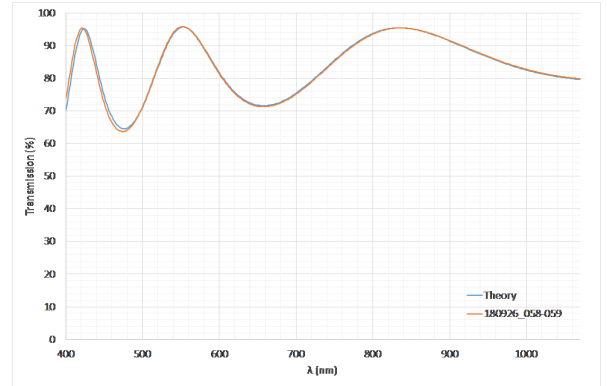


Figure S8: The fabrication process of multilayer MM nano-cuboids. The legend shows the color coding for different material layers, i.e., SiO₂ (green), Nb₂O₅ (light blue), Cr (gray), resist (orange), and Si (dark blue). (a) Thorough cleaning of a Si substrate. (b) Deposition of a Cr sacrificial layer by electron beam evaporation. (c) Plasma-assisted reactive magnetron sputtering deposition of a Nb₂O₅/SiO₂ multilayer stack. (d) Spin-coating of a layer of positive electron beam resist. (e) Patterning of the resist layer with electron beam lithography. (f) Deposition of a Cr etch mask layer by Ar plasma sputtering. (g) Lift-off to finalize the Cr etch mask through removal of the unwanted Cr on non-patterned region by adhesive tape and the subsequent removal of the remaining resist layer by heated resist stripper solution. (h) Etching into the multilayer structure by reactive ion etching. (i) Removal of the top Cr etch mask layer and the bottom sacrificial Cr layer at the same time by dipping the sample into Cr wet etchant solution (dark yellow). (j) First washing of the sample to remove the Cr etchant by dipping the sample into ample amount of DI water (which turns into light yellow). (k) Second washing of the sample to completely remove Cr etchant by dipping the sample into ample amount of DI water (whose color remains the same as that of fresh DI), without any agitation. (l) Harvesting the nano-cuboid particles by submerging the sample into a DI water-filled plastic tube and vortexing for 30 s. Then the remaining Si substrate is removed from the tube, leaving the nano-cuboid particle solution only in the tube.

(a)



(b)



(c)

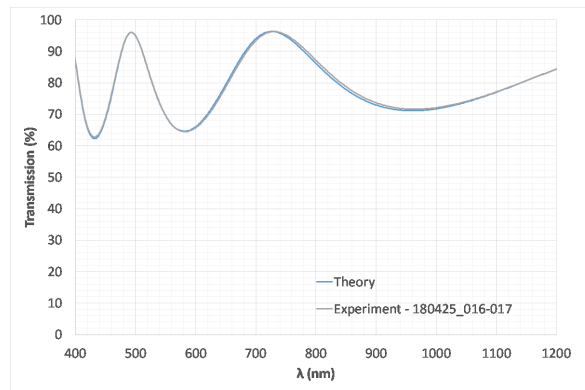


Figure S9: The optical transmission as a function of light wavelength, for the $\text{Nb}_2\text{O}_5/\text{SiO}_2$ multilayer stacks deposited on silica reference substrates by plasma-assisted reactive magnetron sputtering (HELIOS, Bühler). Three multilayer stacks with different combinations of material filling ratio and width have been deposited and measured, including (a) wafer A ($\rho = 0.3$, $W = 300$ nm), (b) wafer B ($\rho = 0.3$, $W = 400$ nm), and (c) wafer C ($\rho = 0.5$, $W = 300$ nm). To precisely control the thickness of each layer, we use in-situ monitoring, i.e., measuring the evolution of the optical transmission at 410 nm-wavelength through a silica reference sample during deposition. The reference sample is pre-coated with a 58 nm-thick Nb_2O_5 layer in the sputtering deposition chamber. Then, the Cr-coated Si substrate is added into the same chamber via a load-lock chamber and coated with a multilayer stack as designed (Table. S1). After the completion of the multilayer deposition, we measure the transmission of the reference sample over a wide range of light wavelength that includes 1064 nm using a spectrophotometer (Lambda 1050, Perkin Elmer). The measured transmission curves show excellent agreement with the theoretical curves, resulting in the error on the thickness of each layer not exceeding ~ 1 nm. These measurements report the refractive index n of each consisting material at 1064 nm ($n = 1.4677$ for SiO_2 ; $n = 2.2590$ for Nb_2O_5).

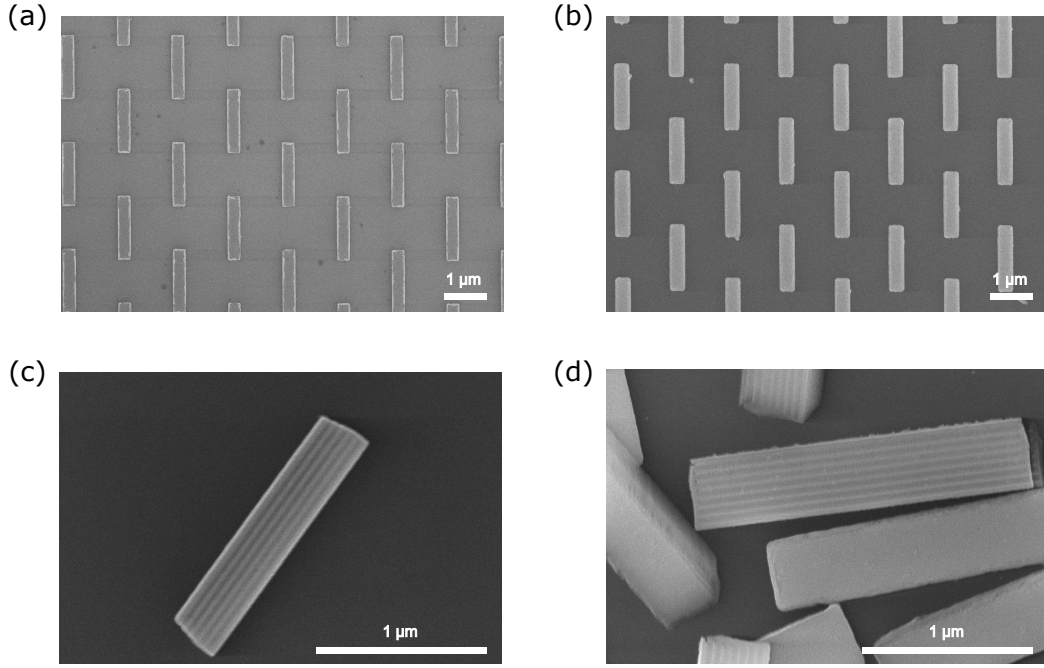


Figure S10: The scanning electron microscopy (SEM) images of the fabricated multilayer MM nano-cuboids. The multilayer particles are patterned in a hexagonal array (with the gap size of $1 \mu\text{m}$) as shown in the top-view images recorded (a) after lift-off process and (b) after reactive ion etching (RIE) process. For both images, Cr etch mask layer exists on top of the particles, and the shown particles have designed dimensions of $W = 300 \text{ nm}$, $AR = 5$. The harvested multilayer particles can be randomly dispersed on a Si substrate for further observations. We show two nano-cuboid batches with optimal height for the maximized torque transfer efficiency, i.e., (c) batch C5 ($\rho = 0.5$, $W = 300 \text{ nm}$, $AR = 5$) and (d) batch B5 ($\rho = 0.3$, $W = 400 \text{ nm}$, $AR = 5$). From these high magnification images showing the side of nano-cuboids, the multilayer structures of Nb_2O_5 (brighter region) and SiO_2 (darker region) are clearly visible. Notably, the particle with $\rho = 0.5$ (C5) shows indeed 1:1 ratio of two consisting materials in panel (c), while the particle with $\rho = 0.3$ (B5) has SiO_2 layers thicker than Nb_2O_5 layers.

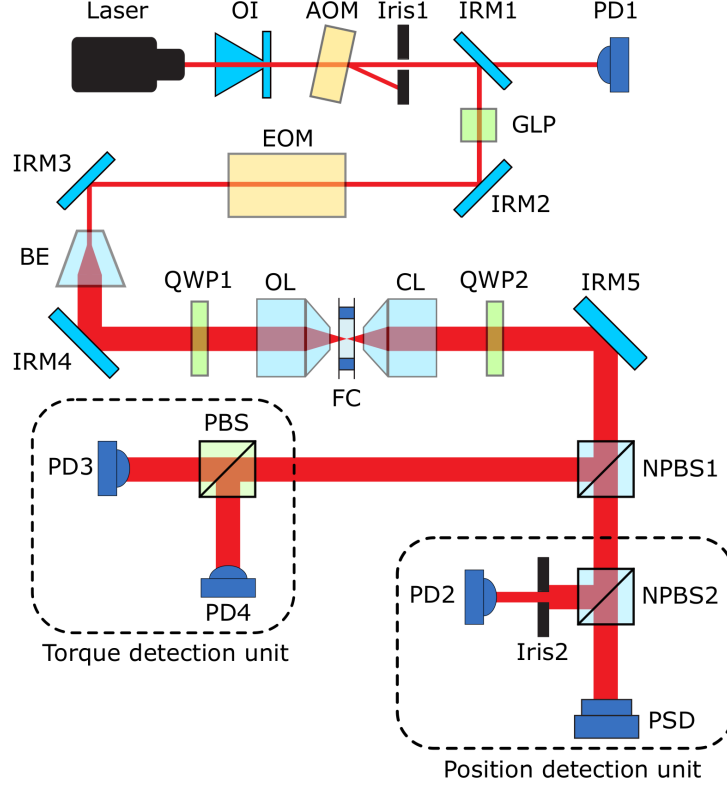


Figure S11: The schematic of the optical torque wrench (OTW) setup. The 1064 nm-wavelength trapping laser beam path is displayed as red solid lines, whose width represents the beam diameter (not to scale). The list of components are as follows: diode-pumped solid-state continuous wave TEM₀₀ 1064 nm laser (Laser), optical isolator (OI), beam expander (BE), infrared mirror (IRM1–5), Iris (Iris1–2), polarizing beam splitter (PBS), 50:50 non-polarizing beam splitter (NPBS1–2), Glan laser polarizer (GLP), quarter-wave plate (QWP1–2), high-speed InGaAs photodiode (PD1–4), position-sensitive detector (PSD), acousto-optic modulator (AOM), electro-optic modulator (EOM), objective lens (OL), condenser lens (CL), flow cell (FC). Both OL and CL are the identical water-immersion lenses with NA of 1.2 and magnification of 60 \times . The color coding for the optics parts is set as dark blue (detectors; PD, PSD), light blue (standard optics: OI, IRM, BE, OL, CL, NPBS), green (polarization optics: GLP, QWP, PBS), and yellow (active optics; AOM, EOM).

The configuration of the OTW setup. The initial part of the beam path is for conditioning the laser beam regarding power, polarization state, and beam diameter. The laser beam is coupled with OI to prevent possible damage to the laser head in case of any intense backscattering events. The AOM and PD1 consist a feedback loop which stabilizes intensity fluctuation of the laser beam. The Iris1 selects only the 0th order output beam and blocks the 1st order output beam from the AOM. The GLP increases the extinction ratio (1 : 10⁵) between *p*- and *s*- polarization components, before entering into EOM for polarization modulation. The beam diameter is increased by the BE to properly fill the back aperture of OL. The beam is tightly focused by OL to effectively trap particles within FC. The beam is then collected by CL and relayed to the analysis units. In this beam path around FC, QWP1 is to send a linearly polarized beam (whose direction is rotatable by EOM) to the optical trap, and QWP2 is to measure transferred angular momentum [54] in the torque detection unit with PBS and PD3–4. In the position detection unit, the *x*- and *y*-positions of the trapped particle are detected by PSD while the *z*-position is detected by PD4 with Iris2 (whose opening is optimized to properly capture the Gouy phase shift [56]). The optical force is then deduced from the measured particle position. This separated detection permits simultaneous optimization for both radial and axial measurements as they have conflicting requirements for iris opening [22]. For high-precision measurements, noise from various sources needs to be blocked or suppressed. In this setup, the laser beam path is enclosed by metallic tubes and the setup is enclosed in a box made of thick plates to prevent turbulent air currents and acoustic noise. Further, every PD is powered by a lead battery to reduce interferences from high-frequency electrical noise. In addition, the AOM is operated at only low RF power to avoid excess heating, to prevent instrumental drift that appears as a large amount of low-frequency noise [50].

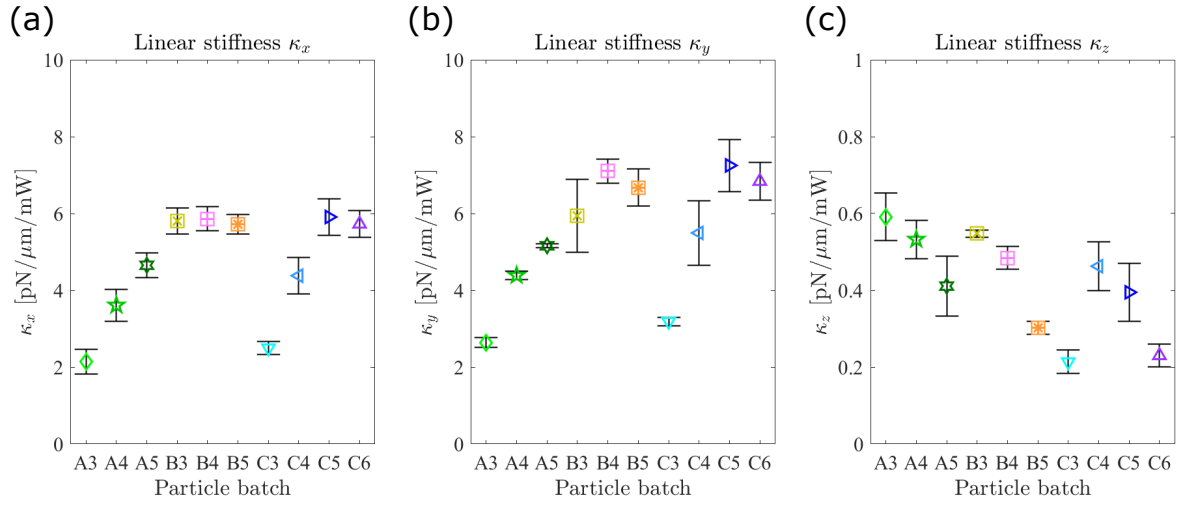


Figure S12: The OTW-measured linear stiffness values of multilayer MM nano-cuboids. For the entire ten batches of nano-cuboids (from A3 to C6), the measurement results of (a) the lateral stiffness along the x -axis (κ_x), (b) the lateral stiffness along the y -axis (κ_y), and (c) the axial stiffness (κ_z) are shown (empty symbols and errorbars denote the mean and the standard deviation (mean \pm S.D.) of each batch, respectively; the same shape and color coding as shown in **Fig. 2**).

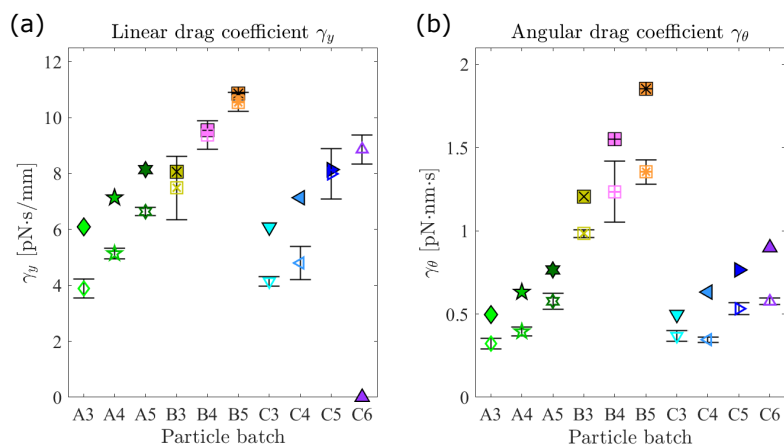


Figure S13: The OTW-measured linear and angular drag coefficients of multilayer MM nano-cuboids, compared with the FEM-calculated values. For the entire ten batches of nano-cuboids (from A3 to C6), the measurement results of (a) the linear drag (γ_y) and (b) the angular drag (γ_θ) are shown (empty symbols and errorbars denote the mean and the standard deviation (mean \pm S.D.) of each batch, respectively), together with the corresponding FEM-predicted values (filled symbols). The shape and color coding of the symbols are the same as shown in **Fig. 2**.

Table S1: The thickness of each consisting layer in fabrication of the Nb₂O₅/SiO₂ multilayer stacks for wafer A, B, and C. The thickness of the unit layer-pair is 50 nm for all wafers and each layer thickness is determined by the material filling ratio ($\rho = 0.3$ for wafer A and B; $\rho = 0.5$ for wafer C). In total, six and eight layer-pairs are used for $W = 300$ nm (wafer A and C) and $W = 400$ nm (wafer B), respectively. To make symmetric particles, the first and the last layers are always SiO₂ layers with the thickness that is a half of the single SiO₂ layer in middle. In common, the multilayer is deposited by plasma-assisted reactive magnetron sputtering onto the sacrificial Cr layer (100 nm-thick) on top of Si wafer ([Methods](#)).

		Wafer A	Wafer B	Wafer C
Layer no.	Material	Thickness /nm	Thickness /nm	Thickness /nm
1	SiO ₂	17.5	17.5	12.5
2	Nb ₂ O ₅	15	15	25
3	SiO ₂	35	35	25
4	Nb ₂ O ₅	15	15	25
5	SiO ₂	35	35	25
6	Nb ₂ O ₅	15	15	25
7	SiO ₂	35	35	25
8	Nb ₂ O ₅	15	15	25
9	SiO ₂	35	35	25
10	Nb ₂ O ₅	15	15	25
11	SiO ₂	35	35	25
12	Nb ₂ O ₅	15	15	25
13	SiO ₂	17.5	35	12.5
14	Nb ₂ O ₅		15	
15	SiO ₂		35	
16	Nb ₂ O ₅		15	
17	SiO ₂		17.5	
	Total	300	400	300

Table S2: The FEM-calculated and OTW-measured linear and angular trapping parameters of multilayer MM nano-cuboids. For all nano-cuboid batches (A3–C6), both experimentally (mean, standard deviation (SD)) and numerically obtained (cal.) results for drag (γ), stiffness (κ), and response time (t_c ; assuming 100 mW of input beam power) are shown. Also, the number of all measured particles (which are used to calculate the mean and SD) from each batch is shown. For angular trapping, the averaged maximal torque (τ_o) and rotation frequency (f_o) at 100 mW beam power (scaled from the actually used 92 mW for rapid interpretation) are also shown. The experimental values are obtained by measuring $N = 3 - 7$ nano-cuboids per batch.

Parameter	Unit	A3	A4	A5	B3	B4	B5	C3	C4	C5	C6
γ_y (mean)	pN·s/mm	3.9	5.1	6.6	7.5	9.4	10.6	4.1	4.8	8.0	8.9
γ_y (SD)	pN·s/mm	0.3	0.2	0.1	1.0	0.4	0.3	0.2	0.5	0.8	0.5
γ_y (cal.)	pN·s/mm	6.1	7.1	8.1	8.1	9.5	10.9	6.1	7.1	8.1	0.0
κ_y (mean)	pN/ μ m/mW	2.6	4.4	5.2	5.9	7.1	6.7	3.2	5.5	7.3	6.8
κ_y (SD)	pN/ μ m/mW	0.1	0.1	0.0	0.8	0.3	0.4	0.1	0.8	0.6	0.5
κ_y (cal.)	pN/ μ m/mW	9.8	10.8	10.9	8.8	6.5	5.2	9.3	10.9	11.0	10.7
$t_{c,y}$ (mean)	μ s (at 100 mW)	14.7	11.7	12.9	12.6	13.2	15.8	13.0	8.7	11.0	13.0
$t_{c,y}$ (SD)	μ s (at 100 mW)	1.3	0.4	0.3	2.4	0.8	1.1	0.6	1.5	1.5	1.1
$t_{c,y}$ (cal.)	μ s (at 100 mW)	6.2	6.6	7.4	9.2	14.7	20.9	6.6	6.5	7.4	0.0
N_y		6	3	6	4	4	5	5	5	6	7
γ_θ (mean)	pN·nm·s	0.32	0.39	0.58	0.98	1.23	1.35	0.37	0.35	0.53	0.58
γ_θ (SD)	pN·nm·s	0.03	0.02	0.04	0.02	0.16	0.06	0.03	0.02	0.03	0.02
γ_θ (cal.)	pN·nm·s	0.50	0.63	0.76	1.21	1.55	1.85	0.50	0.63	0.76	0.90
κ_θ (mean)	pN·nm/rad/mW	133	186	213	282	317	350	203	249	283	288
κ_θ (SD)	pN·nm/rad/mW	6	7	13	6	4	6	6	6	5	5
κ_θ (cal.)	pN·nm/rad/mW	271	338	380	519	548	548	374	467	509	519
$t_{c,\theta}$ (mean)	μ s (at 100 mW)	24.3	21.2	27.1	34.9	38.9	38.6	18.1	13.9	18.8	19.9
$t_{c,\theta}$ (SD)	μ s (at 100 mW)	2.4	1.4	2.6	1.0	5.2	2.0	1.5	0.7	1.1	0.7
$t_{c,\theta}$ (cal.)	μ s (at 100 mW)	18.3	18.7	20.1	23.2	28.3	33.8	13.3	13.5	15.0	17.3
τ_o	nN·nm (at 100 mW)	6.6	9.3	10.6	14.1	15.9	17.5	10.2	12.4	14.2	14.4
f_o	kHz (at 100 mW)	3.3	3.8	2.9	2.3	2.0	2.1	4.4	5.7	4.2	4.0
N_θ		5	3	5	4	5	5	6	6	4	7